Beam-energy-dependent two-pion interferometry and the freeze-out eccentricity of pions measured in heavy ion collisions at the STAR detector

L. Adamczyk *et al.* (STAR Collaboration)

Beam energy dependent two-pion interferometry and the freeze-out eccentricity of pions in heavy ion collisions at STAR

L. Adamczyk,[1] J. K. Adkins,[23] G. Agakishiev,[21] M. M. Aggarwal,[35] Z. Ahammed,[54] I. Alekseev,[19] J. Alford,[22] C. D. Anson,[32] A. Aparin,[21] D. Arkhipkin,[4] E. C. Aschenauer,[4] G. S. Averichev,[21] A. Banerjee,[54] D. R. Beavis,[4] R. Bellwied,[50] A. Bhasin,[20] A. K. Bhati,[35] P. Bhattarai,[49] H. Bichsel,[56] J. Bielcik,[13] J. Bielcikova,[14] L. C. Bland,[4] I. G. Bordyuzhin,[19] W. Borowski,[46] J. Bouchet,[22] A. V. Brandin,[30] S. G. Brovko,[6] S. Bültmann,[33] I. Bunzarov,[21] T. P. Burton,[4] J. Butterworth,[42] H. Caines,[58] M. Calderón de la Barca Sánchez,[6] D. Cebra,[6] R. Cendejas,[36] M. C. Cervantes,[48] P. Chaloupka,[13] Z. Chang,[48] S. Chattopadhyay,[54] H. F. Chen,[43] J. H. Chen,[45] L. Chen,[9] J. Cheng,[51] M. Cherney,[12] A. Chikanian,[58] W. Christie,[4] J. Chwastowski,[37] M. J. M. Codrington,[49] G. Contin,[26] J. G. Cramer,[56] H. J. Crawford,[5] X. Cui,[43] S. Das,[16] A. Davila Leyva,[49] L. C. De Silva,[12] R. R. Debbe,[4] T. G. Dedovich,[21] J. Deng,[44] A. A. Derevschikov,[38] R. Derradi de Souza,[8] S. Dhamija,[18] B. di Ruzza,[4] L. Didenko,[4] C. Dilks,[36] F. Ding,[6] P. Djawotho,[48] X. Dong,[26] J. L. Drachenberg,[53] J. E. Draper,[6] C. M. Du,[25] L. E. Dunkelberger,[7] J. C. Dunlop,[4] L. G. Efimov,[21] J. Engelage,[5] K. S. Engle,[52] G. Eppley,[42] L. Eun,[26] O. Evdokimov,[10] O. Eyser,[4] R. Fatemi,[23] S. Fazio,[4] J. Fedorisin,[21] P. Filip,[21] E. Finch,[58] Y. Fisyak,[4] C. E. Flores,[6] C. A. Gagliardi,[48] D. R. Gangadharan,[32] D. Garand,[39] F. Geurts,[42] A. Gibson,[53] M. Girard,[55] S. Gliske,[2] L. Greiner,[26] D. Grosnick,[53] D. S. Gunarathne,[47] Y. Guo,[43] A. Gupta,[20] S. Gupta,[20] W. Guryn,[4] B. Haag,[6] A. Hamed,[48] L-X. Han,[45] R. Haque,[31] J. W. Harris,[58] S. Heppelmann,[36] A. Hirsch,[39] G. W. Hoffmann,[49] D. J. Hofman,[10] S. Horvat,[58] B. Huang,[4] H. Z. Huang,[7] X. Huang,[51] P. Huck,[9] T. J. Humanic,[32] G. Igo,[7] W. W. Jacobs,[18] H. Jang,[24] E. G. Judd,[5] S. Kabana,[46] D. Kalinkin,[19] K. Kang,[51] K. Kauder,[10] H. W. Ke,[4] D. Keane,[22] A. Kechechyan,[21] A. Kesich,[6] Z. H. Khan,[10] D. P. Kikola,[55] I. Kisel,[15] A. Kisiel,[55] D. D. Koetke,[53] T. Kollegger,[15] J. Konzer,[39] I. Koralt,[33] L. K. Kosarzewski,[55] L. Kotchenda,[30] A. F. Kraishan,[47] P. Kravtsov,[30] K. Krueger,[2] I. Kulakov,[15] L. Kumar,[31] R. A. Kycia,[11] M. A. C. Lamont,[4] J. M. Landgraf,[4] K. D. Landry,[7] J. Lauret,[4] A. Lebedev,[4] R. Lednicky,[21] J. H. Lee,[4] M. J. LeVine,[4] C. Li,[43] W. Li,[45] X. Li,[39] X. Li,[47] Y. Li,[51] Z. M. Li,[9] M. A. Lisa,[32] F. Liu,[9] T. Ljubicic,[4] W. J. Llope,[42] M. Lomnitz,[22] R. S. Longacre,[4] X. Luo,[9] G. L. Ma,[45] Y. G. Ma,[45] D. M. M. D. Madagodagettige Don,[12] D. P. Mahapatra,[16] R. Majka,[58] S. Margetis,[22] C. Markert,[49] H. Masui,[26] H. S. Matis,[26] D. McDonald,[50] T. S. McShane,[12] N. G. Minaev,[38] S. Mioduszewski,[48] B. Mohanty,[31] M. M. Mondal,[48] D. A. Morozov,[38] M. K. Mustafa,[26] B. K. Nandi,[17] Md. Nasim,[31] T. K. Nayak,[54] J. M. Nelson,[3] G. Nigmatkulov,[30] L. V. Nogach,[38] S. Y. Noh,[24] J. Novak,[29] S. B. Nurushev,[38] G. Odyniec,[26] A. Ogawa,[4] K. Oh,[40] A. Ohlson,[58] V. Okorokov,[30] E. W. Oldag,[49] D. L. Olvitt Jr.,[47] M. Pachr,[13] B. S. Page,[18] S. K. Pal,[54] Y. X. Pan,[7] Y. Pandit,[10] Y. Panebratsev,[21] T. Pawlak,[55] B. Pawlik,[34] H. Pei,[9] C. Perkins,[5] W. Peryt,[55] P. Pile,[4] M. Planinic,[59] J. Pluta,[55] N. Poljak,[59] K. Poniatowska,[55] J. Porter,[26] A. M. Poskanzer,[26] N. K. Pruthi,[35] M. Przybycien,[1] P. R. Pujahari,[17] J. Putschke,[57] H. Qiu,[26] A. Quintero,[22] S. Ramachandran,[23] R. Raniwala,[41] S. Raniwala,[41] R. L. Ray,[49] C. K. Riley,[58] H. G. Ritter,[26] J. B. Roberts,[42] O. V. Rogachevskiy,[21] J. L. Romero,[6] J. F. Ross,[12] A. Roy,[54] L. Ruan,[4] J. Rusnak,[14] O. Rusnakova,[13] N. R. Sahoo,[48] P. K. Sahu,[16] I. Sakrejda,[26] S. Salur,[26] J. Sandweiss,[58] E. Sangaline,[6] A. Sarkar,[17] J. Schambach,[49] R. P. Scharenberg,[39] A. M. Schmah,[26] W. B. Schmidke,[4] N. Schmitz,[28] J. Seger,[12] P. Seyboth,[28] N. Shah,[7] E. Shahaliev,[21] P. V. Shanmuganathan,[22] M. Shao,[43] B. Sharma,[35] W. Q. Shen,[45] S. S. Shi,[26] Q. Y. Shou,[45] E. P. Sichtermann,[26] R. N. Singaraju,[54] M. J. Skoby,[18] D. Smirnov,[4] N. Smirnov,[58] D. Solanki,[41] P. Sorensen,[4] H. M. Spinka,[2] B. Srivastava,[39] T. D. S. Stanislaus,[53] J. R. Stevens,[27] R. Stock,[15] M. Strikhanov,[30] B. Stringfellow,[39] M. Sumbera,[14] X. Sun,[26] X. M. Sun,[26] Y. Sun,[43] Z. Sun,[25] B. Surrow,[47] D. N. Svirida,[19] T. J. M. Symons,[26] M. A. Szelezniak,[26] J. Takahashi,[8] A. H. Tang,[4] Z. Tang,[43] T. Tarnowsky,[29] J. H. Thomas,[26] A. R. Timmins,[50] D. Tlusty,[14] M. Tokarev,[21] S. Trentalange,[7] R. E. Tribble,[48] P. Tribedy,[54] B. A. Trzeciak,[13] O. D. Tsai,[7] J. Turnau,[34] T. Ullrich,[4] D. G. Underwood,[2] G. Van Buren,[4] G. van Nieuwenhuizen,[27] M. Vandenbroucke,[47] J. A. Vanfossen, Jr.,[22] R. Varma,[17] G. M. S. Vasconcelos,[8] A. N. Vasiliev,[38] R. Vertesi,[14] F. Videbæk,[4] Y. P. Viyogi,[54] S. Vokal,[21] A. Vossen,[18] M. Wada,[49] F. Wang,[39] G. Wang,[7] H. Wang,[4] J. S. Wang,[25] X. L. Wang,[43] Y. Wang,[51] Y. Wang,[10] G. Webb,[23] J. C. Webb,[4] G. D. Westfall,[29] H. Wieman,[26] S. W. Wissink,[18] R. Witt,[52] Y. F. Wu,[9] Z. Xiao,[51] W. Xie,[39] K. Xin,[42] H. Xu,[25] J. Xu,[9] N. Xu,[26] Q. H. Xu,[44] Y. Xu,[43] Z. Xu,[4] W. Yan,[51] C. Yang,[43] Y. Yang,[25] Y. Yang,[9] Z. Ye,[10] P. Yepes,[42] L. Yi,[39] K. Yip,[4] I-K. Yoo,[40] N. Yu,[9] Y. Zawisza,[43] H. Zbroszczyk,[55] W. Zha,[43] J. B. Zhang,[9] J. L. Zhang,[44] S. Zhang,[45] X. P. Zhang,[51] Y. Zhang,[43] Z. P. Zhang,[43] F. Zhao,[7] J. Zhao,[9] C. Zhong,[45] X. Zhu,[51] Y. H. Zhu,[45] Y. Zoulkarneeva,[21] and M. Zyzak[15]

(STAR Collaboration)

[1]*AGH University of Science and Technology, Cracow, Poland*
[2]*Argonne National Laboratory, Argonne, Illinois 60439, USA*
[3]*University of Birmingham, Birmingham, United Kingdom*
[4]*Brookhaven National Laboratory, Upton, New York 11973, USA*
[5]*University of California, Berkeley, California 94720, USA*
[6]*University of California, Davis, California 95616, USA*
[7]*University of California, Los Angeles, California 90095, USA*

^{8}Universidade Estadual de Campinas, Sao Paulo, Brazil
^{9}Central China Normal University (HZNU), Wuhan 430079, China
^{10}University of Illinois at Chicago, Chicago, Illinois 60607, USA
^{11}Cracow University of Technology, Cracow, Poland
^{12}Creighton University, Omaha, Nebraska 68178, USA
^{13}Czech Technical University in Prague, FNSPE, Prague, 115 19, Czech Republic
^{14}Nuclear Physics Institute AS CR, 250 68 Řež/Prague, Czech Republic
^{15}Frankfurt Institute for Advanced Studies FIAS, Germany
^{16}Institute of Physics, Bhubaneswar 751005, India
^{17}Indian Institute of Technology, Mumbai, India
^{18}Indiana University, Bloomington, Indiana 47408, USA
^{19}Alikhanov Institute for Theoretical and Experimental Physics, Moscow, Russia
^{20}University of Jammu, Jammu 180001, India
^{21}Joint Institute for Nuclear Research, Dubna, 141 980, Russia
^{22}Kent State University, Kent, Ohio 44242, USA
^{23}University of Kentucky, Lexington, Kentucky, 40506-0055, USA
^{24}Korea Institute of Science and Technology Information, Daejeon, Korea
^{25}Institute of Modern Physics, Lanzhou, China
^{26}Lawrence Berkeley National Laboratory, Berkeley, California 94720, USA
^{27}Massachusetts Institute of Technology, Cambridge, Massachusetts 02139-4307, USA
^{28}Max-Planck-Institut für Physik, Munich, Germany
^{29}Michigan State University, East Lansing, Michigan 48824, USA
^{30}Moscow Engineering Physics Institute, Moscow Russia
^{31}National Institute of Science Education and Research, Bhubaneswar 751005, India
^{32}Ohio State University, Columbus, Ohio 43210, USA
^{33}Old Dominion University, Norfolk, Virginia 23529, USA
^{34}Institute of Nuclear Physics PAN, Cracow, Poland
^{35}Panjab University, Chandigarh 160014, India
^{36}Pennsylvania State University, University Park, Pennsylvania 16802, USA
^{37}Institute of Nuclear Physics Polish Academy of Sciences, PL-31342 Krakow, Poland
^{38}Institute of High Energy Physics, Protvino, Russia
^{39}Purdue University, West Lafayette, Indiana 47907, USA
^{40}Pusan National University, Pusan, Republic of Korea
^{41}University of Rajasthan, Jaipur 302004, India
^{42}Rice University, Houston, Texas 77251, USA
^{43}University of Science and Technology of China, Hefei 230026, China
^{44}Shandong University, Jinan, Shandong 250100, China
^{45}Shanghai Institute of Applied Physics, Shanghai 201800, China
^{46}SUBATECH, Nantes, France
^{47}Temple University, Philadelphia, Pennsylvania 19122, USA
^{48}Texas A&M University, College Station, Texas 77843, USA
^{49}University of Texas, Austin, Texas 78712, USA
^{50}University of Houston, Houston, Texas 77204, USA
^{51}Tsinghua University, Beijing 100084, China
^{52}United States Naval Academy, Annapolis, Maryland, 21402, USA
^{53}Valparaiso University, Valparaiso, Indiana 46383, USA
^{54}Variable Energy Cyclotron Centre, Kolkata 700064, India
^{55}Warsaw University of Technology, Warsaw, Poland
^{56}University of Washington, Seattle, Washington 98195, USA
^{57}Wayne State University, Detroit, Michigan 48201, USA
^{58}Yale University, New Haven, Connecticut 06520, USA
^{59}University of Zagreb, Zagreb, HR-10002, Croatia
(Dated: April 6, 2015)

We present results of analyses of two-pion interferometry in Au+Au collisions at $\sqrt{s_{NN}}$ = 7.7, 11.5, 19.6, 27, 39, 62.4 and 200 GeV measured in the STAR detector as part of the RHIC Beam Energy Scan program. The extracted correlation lengths (HBT radii) are studied as a function of beam energy, azimuthal angle relative to the reaction plane, centrality, and transverse mass (m_T) of the particles. The azimuthal analysis allows extraction of the eccentricity of the entire fireball at kinetic freeze-out. The energy dependence of this observable is expected to be sensitive to changes in the equation of state. A new global fit method is studied as an alternate method to directly measure the parameters in the azimuthal analysis. The eccentricity shows a monotonic decrease with beam energy that is qualitatively consistent with the trend from all model predictions and quantitatively consistent with a hadronic transport model.

I. INTRODUCTION

The Beam Energy Scan program performed at the Relativistic Heavy Ion Collider (RHIC) in 2010 and 2011 was designed to map features expected to appear in the QCD phase diagram [1]. At the highest RHIC energies evidence suggests that the matter formed in heavy ion collisions is a hot, strongly coupled fluid of deconfined quarks and gluons (sQGP) [2–5], with rather low chemical potential, μ_B. The nature of this phase transition is likely a smooth, rapid cross-over transition [6–9]. As the beam energy is lowered, the matter produced near mid-rapidity evolves through regions of the phase diagram at larger μ_B. At higher chemical potentials there are predictions from lattice calculations of a change to a first-order phase transition with an associated latent heat [10–16] and a critical point at some intermediate chemical potential [17]. The relative amounts of time the matter spends in an sQGP, mixed or hadronic phase may imprint a signal on observables that are sensitive to the equation of state [18]. It is important, therefore, to study such observables as a function of beam energy both to search for possible non-monotonic behavior (which could indicate interesting physical changes in some aspect of the collisions) and to provide more stringent experimental guidance to theory and models. The sizes and shapes that describe the matter produced in the collisions at freeze-out provide just this type of observable [19].

Results of two-pion interferometry analyses (often referred to as HBT analyses) are presented in this paper as a function of beam energy. Hanbury Brown and Twiss invented the intensity interferometry technique to measure sizes of nearby stars [20]. The technique was extended to particle physics [21] to study angular distributions of pion pairs in $p\bar{p}$ annihilations, finding that quantum statistics caused an enhancement in pairs with low relative momentum. In subsequent HBT analyses the method has evolved into a precision tool for measuring space-time properties of the regions of homogeneity at kinetic freeze-out in heavy ion collisions [22]. Two-pion interferometry yields HBT radii that describe the geometry of these regions of homogeneity (regions that emit correlated pion pairs). The observation that HBT radii increase for more central collisions is attributed to the increasing volume of the source, an example of how HBT can probe spatial sizes and shapes [22]. In addition to the spatial shape and size of these regions from which particle pairs are emitted, space-momentum correlations induced by collective (and anisotropic) flow [23] may imprint patterns on the results. For instance, the HBT radii exhibit a systematic decrease with mean pair transverse momentum, k_T, which has been attributed to transverse and longitudinal flow [23, 24]. The presence of flow induces space-momentum correlations so that the size of the regions emitting particles does not correspond to the entire fireball created in a collision [22–24]. In standard HBT analyses, integrated over azimuthal angle relative to the reaction plane, the extracted source sizes correspond only to some smaller region of the total volume; the higher the transverse momentum, k_T,

the smaller the radii describing the volume emitting the particles [22]. However, in HBT analyses performed relative to the reaction plane, sinusoidal variations in the shape of these smaller source regions can be connected to the overall shape of the entire fireball [23, 24].

Previous HBT analyses from various experiments have led to a large world data set for standard, non-azimuthal HBT results at AGS [25–27] and SPS [28–31], as well as top RHIC energies [32–35], and at the LHC [36–38]. In contrast, only a few azimuthal HBT results have been reported previously by E895 [39], STAR [40], PHENIX [41], and CERES [42]. While the results suggested possible non-monotonic behavior in the freeze-out shape of the collisions with a minimum appearing around a collision energy per nucleon of 17.3 GeV, the sparse amount of data coming from several different experiments could not allow one to draw a definite conclusion [42]. In this paper, the results of azimuthally integrated HBT analyses are placed in the context of the world data set reproducing the low energy and high energy results and filling in the intermediate energy region with results from a single detector and identical analysis techniques. The azimuthally differential HBT results are also presented across this wide range of energies allowing extraction of the beam energy dependence of the transverse eccentricity at freeze-out.

In the case of the azimuthally differential analysis, a new global fit method is developed. The technique, described in this paper, uses a Gaussian parameterization. However, several correlation functions constructed in azimuthal bins relative to the reaction plane are fit simultaneously. This allows direct extraction of Fourier coefficients that describe the observed sinusoidal variations in the shape of the regions of homogeneity that emit pion pairs. This technique avoids correlated errors that arise from a correction for finite-bin-width and event plane resolution effects and it is more robust in some cases where statistics and event plane resolutions are low. The global fit method provides the most reliable estimate of the shape of the fireball at kinetic freeze-out which, as described in the next section, is used to search for a change in the type of phase transition at lower energies. The experimental results of this study are presented in Sec. VI B 3.

II. COLLISION EVOLUTION AND FREEZE-OUT SHAPE

A primary theme explored in this analysis is the connection between the type of phase transition the system experiences and the shape of the collision during kinetic freeze-out. Therefore, in this section we explore the relationship between the underlying physics and the final shape achieved in the collisions. In non-central collisions, the second order anisotropy of the participant zone (in the transverse plane) is an ellipse extended out of the reaction plane (the plane containing the impact parameter and beam direction). Initial state fluctuations in positions of participant nucleons may cause deviations from a precise elliptical shape [43]. Nevertheless, the initial

shape is approximately elliptical and can be estimated using Monte Carlo Glauber calculations. Due to the anisotropic shape and the speed of sound, $c_s^2 = \partial p / \partial e$ (where p is pressure and e is energy density), larger initial pressure gradients appear along the short axis. These stronger in-plane pressure gradients drive preferential in-plane expansion, thereby reducing the eccentricity. The system must evolve to a less out-of-plane extended freeze-out shape. Longer lifetimes, stronger pressure gradients, or both, would lead to expansion to an even more round or even in-plane extended (negative eccentricity) shape at kinetic freeze-out. It would be expected that increasing the beam energy would lead to longer lifetimes and pressure gradients and so a monotonically decreasing excitation function for the freeze-out eccentricity would be expected [19]. In fact, all transport and hydrodynamic models predict a monotonic decrease in the energy ranges studied here.

There is, however, another consideration related to the equation of state. If the nature of the phase transition changes from a smooth cross-over at high energy to a first-order transition at lower energy, the matter will evolve through a mixed-phase regime (associated with a latent heat) during which the pressure gradients vanish ($c_s^2 = 0$). Outside of a mixed-phase regime, the equation of state has even stronger pressure gradients ($c_s^2 = 1/3$) in the sQGP phase than the hadronic phase ($c_s^2 = 1/6$) [44, 45]. As the collision energy is varied, the collisions evolve along different trajectories through the T-μ_B phase diagram. At low energy the system may evolve through a first-order phase transition and the length of time spent in the various phases may alter the amount of expansion that takes place prior to freeze-out [45]. It is possible that a non-monotonic freeze-out shape might be observed as a result. In fact, it was speculated in [19] that the possible minimum observed in the previously available freeze-out eccentricity measurements might be caused by entrance into a mixed-phase regime around a minimum, followed by a maximum at higher energy above which the system achieves complete deconfinement (and the strong pressure gradients reappear). Measuring the energy dependence of the freeze-out shape therefore allows one to probe interesting physics related to both the equation of state and dynamical processes that drive the evolution of the collisions.

III. EXPERIMENTAL SETUP AND EVENT, TRACK, AND PAIR SELECTIONS

A. STAR detector

The STAR detector [46] was used to reconstruct Au+Au collisions provided at $\sqrt{s_{NN}}$ = 7.7, 11.5, 19.6, 27, 39, 62.4 and 200 GeV as part of a first phase of the Beam Energy Scan program. The main detector used in this analysis is the Time Projection Chamber (TPC) [47, 48], which allows reconstruction of the momentum of charged particles used for event plane determination, including the charged pions used in the HBT analyses. The TPC covers the pseudorapidity range $|\eta| < 1$ and has full 2π azimuthal acceptance. It is located inside a 0.5 T solenoidal magnetic field for all energies to aid in identi-

$\sqrt{s_{NN}}$ (GeV)	$|V_Z|$ (cm)	N_{events} (10^6)
7.7	< 70	3.9
11.5	< 50	10.7
19.6	< 30	15.4
27	< 30	30.8
39	< 30	8.8
62.4	< 30	10.1
200	< 30	11.6

TABLE I: Number of analyzed events and z-vertex range, V_Z, at each energy.

fying the charge, momentum, and species of each track. Zero Degree Calorimeters, Beam-Beam Counters and/or Vertex Position Detectors, located at large rapidities near the beam line, were tuned online to collect high statistics, minimum bias data sets at each energy. Measuring coincidences of spectator particles in the subsystems allows selection of collisions that occur near the center of the detector.

B. Event selection

Events included in the analysis were selected using the reconstructed vertex position. The radial vertex position ($V_R = \sqrt{V_X^2 + V_Y^2}$) was required to be less than 2 cm to reject collisions with the beam pipe. The vertex position along the beam direction, V_Z, was required to be near the center of the detector as summarized in Table I, with larger ranges at 7.7 and 11.5 GeV to maximize statistics. The number of events at each energy used in this analysis are also listed in Table I.

The events were binned in different centrality ranges based on multiplicity as described in [49]. For the azimuthal HBT analysis, data in the 0-5%, 5-10%, 10-20%, 20-30%, and 30-40% centrality bins were used. For the non-azimuthal HBT analysis, additional 40-50%, 50-60% and 60-70% bins were also studied.

C. Particle selection

Tracks were selected in three rapidity ranges: $-1 < y < -0.5$ (backward rapidity), $-0.5 < y < 0.5$ (mid-rapidity), and $0.5 < y < 1$ (forward rapidity). Each track was required to have hits on more than 15 (out of 45 maximum) of the rows of TPC readout pads to ensure good tracks. A requirement on the distance of closest approach (DCA) to the primary vertex, $DCA < 3$ cm, was imposed to reduce contributions from non-primary pions.

Particle identification is accomplished by measuring energy loss in the gas, dE/dx, for each track and comparing to the
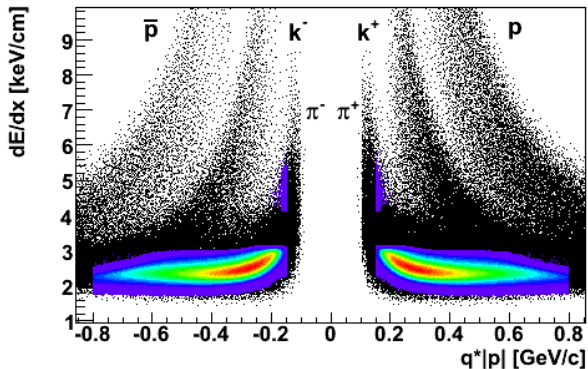
FIG. 1: (Color online) The energy loss in the TPC, dE/dx. The colored region highlights the pions selected for this analysis. The gaps in the colored region at $|p| \approx 0.2$ GeV/c are caused by the cut to eliminate electrons from the analysis in the region where the electron and pion bands overlap. This example is from 0-5% central, 27 GeV Au+Au collisions.

expected value for each species ($i = e^{\pm}, \pi^{\pm}, k^{\pm}, p, \bar{p}$) using the equation

$$n\sigma_i = \frac{1}{\sigma_i} \log\left(\frac{dE/dx_{\text{measured}}}{dE/dx_{\text{expected},i}}\right) \quad (1)$$

where σ_i is the dE/dx resolution of the TPC. Tracks with $|n\sigma_\pi| < 2$ allow identification of pions for use in the analysis. An additional requirement that $|n\sigma_e|$, $|n\sigma_k|$, and $|n\sigma_p| > 2$ supresses contamination from other particles. Additionally, a transverse momentum cut, $0.15 < p_T < 0.8$ GeV/c, further ensures particles come from the region where the pion band is separated from the kaon band. Any contamination is estimated to be less than 1.7% even before the $n\sigma$ cut to reject kaons. Figure 1 demonstrates that these cuts effectively remove particles other than pions.

D. Pair k_T cuts and binning

Similar to previous analyses [33–35, 40] pairs were required to have average transverse pair momenta, $k_T = |\vec{p}_{T1} + \vec{p}_{T2}|/2$, in the range $0.15 < k_T < 0.6$ GeV/c. For the non-azimuthal HBT analyses four k_T bins were used: [0.15,0.25] GeV/c, [0.25,0.35] GeV/c, [0.35,0.45] GeV/c, [0.45,0.6] GeV/c. This binning allows the presentation of results as a function of mean k_T (or $m_T = \sqrt{k_T^2 + m_\pi^2}$) in each bin. These bins yield mean k_T values similar to those in the data from previous analyses allowing direct comparison of certain quantities to previously observed trends.

In earlier azimuthal HBT studies by CERES [42] and STAR [40] the analysis was performed in similar, narrow k_T bins. For an azimuthally differential HBT analysis the statistics are spread across at least four additional azimuthal bins. At the lowest energies this did not allow for sufficient statistics. For instance, the 7.7 GeV dataset has both the fewest number of

events and the lowest multiplicity per event in each centrality bin. Reliable results could not be obtained from data split into both multiple k_T and multiple bins relative to the reaction plane. Instead, a single k_T-integrated analysis was performed using all pairs in the combined range $0.15 < k_T < 0.6$ GeV/c with $\langle k_T \rangle \approx 0.31$ GeV/c. The eccentricity at kinetic freeze-out exhibits a systematic decrease by as much as 0.02 when using a single wide k_T range compared to analyses where results from several narrow k_T ranges are averaged. This is simply because the lowest k_T bin appears to give a slightly smaller eccentricity. When a wide bin is used the results are biased toward the low k_T results due to the much higher statistics of the low k_T pairs. In the earlier analyses, CERES reported a weighted average of results for different k_T bins, while STAR used an average without statistical weights. In any case, to compare the present results as a function of $\sqrt{s_{NN}}$ the same k_T integrated range was used for all energies.

For the azimuthally differential analysis, the pairs were separated into four $45°$ wide azimuthal bins relative to the reaction plane direction using the angle $\Phi = \phi_{\text{pair}} - \psi_2$. The angle of each pair, ϕ_{pair}, is the azimuthal angle of the average pair transverse momentum vector, $\vec{k}_T$, and ψ_2 is the second-order event plane angle defined in the range $[0, \pi]$. This allows measurement of the oscillations of parameters necessary to estimate the freeze-out eccentricity as projected on the transverse plane. A first order analysis could provide additional information at the lowest energies [19, 24]. However, significant additional work is needed to obtain first order results due to complications from relatively low statistics spread across more bins and with much lower first order (compared to second order) event plane resolutions.

IV. ANALYSIS METHOD

A. The correlation function

The experimental correlation function is constructed by forming the distributions of relative momenta, $\vec{q} = (\vec{p}_1 - \vec{p}_2)$. A numerator, $N(\vec{q})$, uses particles from the same event, while a mixed event denominator, $D(\vec{q})$, uses particles from different events. The numerator distribution is driven by two-particle phase space, quantum statistics, and Coulomb interactions, while the denominator reflects only phase space effects. Since quantum statistics and final state interactions are driven by freeze-out geometry [22], the ratio

$$C(\vec{q}) = \frac{N(\vec{q})}{D(\vec{q})} \quad (2)$$

carries geometrical information. In the azimuthally differential analysis, four correlation functions were formed corresponding to four $45°$ wide angular bins relative to the event plane centered at $0°$ (in-plane), $45°$, $90°$ (out-of-plane), and $135°$. The angle between the transverse momentum for each pair and the event plane is used to assign each pair to one of the correlation functions. The denominators were constructed with pairs formed from mixed events. Events were mixed only

with other events in the same centrality bin and with relative z vertex positions of less than 5 cm. For the azimuthally differential case, events were also required to have the estimated reaction plane within $22.5°$, similar to an earlier analysis [40]. Reducing the width of the mixing bins only changes the relative normalizations in the different angular bins but has no effect on the other fit parameters. The correlation functions in this analysis are formed with like-sign pions and the separate distributions for $\pi^+\pi^+$ and $\pi^-\pi^-$ are later combined before fitting since no significant difference between the two cases has been observed.

Detector inefficiency and acceptance effects apply to both the numerator and denominator and so, in taking the ratio to form the correlation function, these effects largely cancel. However, two particle reconstruction inefficiencies allow track splitting and merging effects which are removed as will be described.

A single charged particle track may be reconstructed as two tracks with nearly identical momentum by the tracking algorithm. This so called track splitting can strongly affect correlation measurements by contributing false pairs to the correlation function at small relative momenta, the signal region. The same algorithm, described in [33], to remove split tracks is used in the current analysis. Studies analogous to those in [33] show the same "splitting level" requirement, $SL < 0.6$, is also effective at removing track splitting effects in the current data sets.

On the other hand, two particles with small relative momenta can be reconstructed as a single track, thus reducing the measured number of correlated particles. In the following we briefly recapitulate the technique applied for removing track merging effects, detailed in Ref. [33]. If two tracks have hits on the same row of readout pads in the TPC that are too close together, they would appear as a single "merged" hit. Two tracks with such "merged" hits on many of the 45 rows of TPC readout pads are more likely to be reconstructed as a single merged track. For each pair of tracks, the fraction of hits that are close enough so they would appear merged is computed. The allowed fraction of merged hits (FMH) can be reduced until the effect is eliminated. The same algorithm can be applied to track pairs from the numerator and denominator. It was determined that FMH $< 10\%$ reduced track merging effects as much as possible. While this approach eliminates the potentially large effect of track merging, it introduces a systematic uncertainty due to the non-Gaussianess of the correlation function. The azimuthal HBT analysis is more sensitive to the track merging cut and allows the systematic uncertainty associated with this requirement to be estimated in Sec. IV E. Analogous studies to those in [33] using current low energy data sets lead to the same dependence of the radii on FMH, so in the present analyses the same requirement that FMH $< 10\%$ is imposed to remove effects of track merging.

B. Bertsch-Pratt parameterization

The relative pair momentum, $\vec{q}$, is projected onto the Bertsch-Pratt [50–52], out-side-long (or o-s-l), coordinate system so that q_{out} lies along the direction of the average transverse pair momentum, $\vec{k}_T$, while q_{long} lies along the "longitudinal" beam direction, and q_{side} is perpendicular to the other directions and is therefore also in the transverse plane. The relative momentum is expressed in the longitudinal co-moving system (LCMS) in which the longitudinal component of the pair velocity vanishes.

To extract the bulk shape of the particle emitting regions, a Gaussian parameterization is typically used:

$$C(\vec{q}) = (1-\lambda) + K_{\text{Coul}}(q_{\text{inv}})\lambda$$
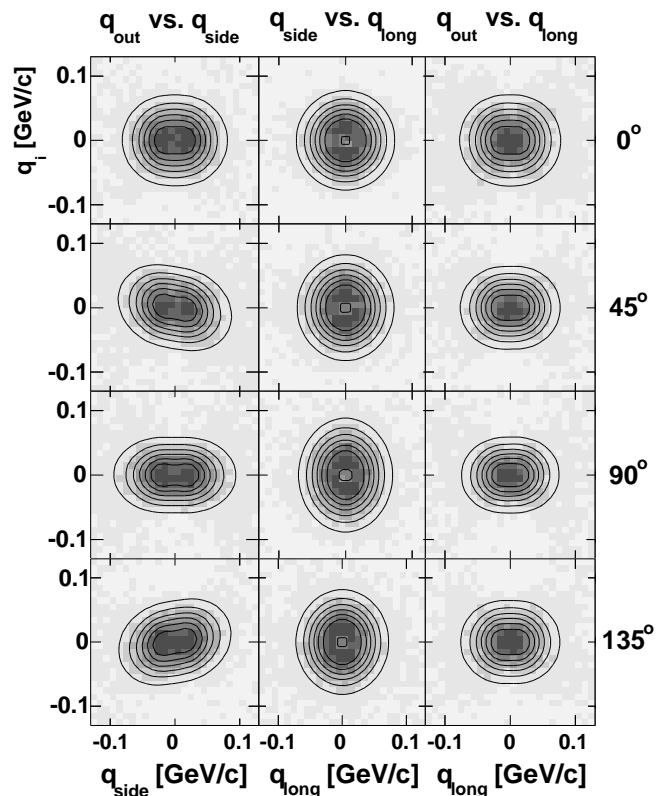$$\times \exp\left(-q_o^2 R_o^2 - q_s^2 R_s^2 - q_l^2 R_l^2 - 2q_o q_s R_{os}^2 - 2q_o q_l R_{ol}^2\right) \quad (3)$$

FIG. 2: Two dimensional projections of a correlation function in the q_o-q_s, q_s-q_l and q_o-q_l planes for like-sign pions at mid-rapidity in 20-30% central, 27 GeV collisions with $0.15 < k_T < 0.6$ GeV/c. All scales are in GeV/c. In each case the third component is projected over ± 0.03 GeV/c. The emission angles relative to the event plane are within $\pm22.5°$ of the bin centers indicated along the right side. The tilt in the q_o-q_s plane is clearly visible. Contour lines represent projections of the corresponding fit.

The λ parameter accounts for non-primary particles that may come from resonance decays and misidentified particles [33]. The parameter R_{ol}^2 in equation 3 is relevant when analyzing rapidity slices not centered at midrapidity [53]. It was not used in [33], which focused exclusively on midrapidity pions. The values of K_{Coul} account for the Coulomb interaction as discussed in the next section. An overall normalization of the

correlation function, also determined during the fitting procedure, scales the correlation function to a value of unity at large values of $|\vec{q}|$.

The R_{ol}^2 term vanishes at mid-rapidity, but becomes positive (negative) at forward (backward) rapidity in both azimuthal and non-azimuthal analyses [52]. For the azimuthally integrated analysis R_{os}^2 vanishes, while in an azimuthally differential analysis a second order sinusoidal variation appears relative to the reaction plane. Parametrically, a non-zero cross term corresponds to a tilt of the correlation function in $\vec{q}$-space. This can be seen clearly in Fig. 2 in the q_{out}-q_{side} plane. At $45°$ there is a tilt resulting in a positive R_{os}^2 cross term. At $135°$ there is an opposite tilt corresponding to a negative R_{os}^2 cross term. The interplay between the cross terms and the inherent non-Gaussianess of the correlation function is discussed later in an appendix, where folding the relative momentum distributions allows covariations in the fit parameters that would strongly affect the results. In this analysis, no folding of $\vec{q}$-space is performed, eliminating this effect.

In the azimuthally differential analysis, several correlation functions are constructed for different angular bins. These are each fit with Eq. 3 to extract the fit parameters. The relationship between these fit parameters describing the regions of homogeneity and the shape of the source region (the collision fireball at kinetic freeze-out) has been described in several references, such as [23, 24, 53], for boost invariant systems.

C. Coulomb interaction

Particles that are nearby in phase space and carry the signal in the correlation function will also experience Coulomb interactions. This effect must be taken into account when extracting the HBT radii. Different methods of accounting for the Coulomb interaction were studied systematically in [33]. This analysis uses the Bowler-Sinyukov method [54, 55]. The Coulomb interaction is computed for each pair with relative momentum components, (q_o, q_s, q_l), that enters the analysis. The average interaction in each (q_o, q_s, q_l) bin is included as a constant, K_{Coul}, in the fit parameterization. The quantity K_{Coul} is the squared Coulomb wave function integrated over the entire spherical Gaussian source. The same radius, 5 fm, is used as in earlier analyses. In Eq. 3, K_{Coul} only applies to the pairs nearby in phase space (the exponential term) and not to other particles accounted for by the $(1 - \lambda)$ term.

In principle, correction for the Coulomb interaction between each particle and the mean field could also be taken into account. However, at the energies studied here, this interaction has been found to be negligible [56, 57].

D. Event plane calculations

The azimuthal analysis requires determining the event plane for each event, including applying appropriate methods to make the event plane distribution uniform [58]. Uncertainty in the event plane reduces the extracted oscillation amplitudes of the HBT radii. The event plane resolutions must
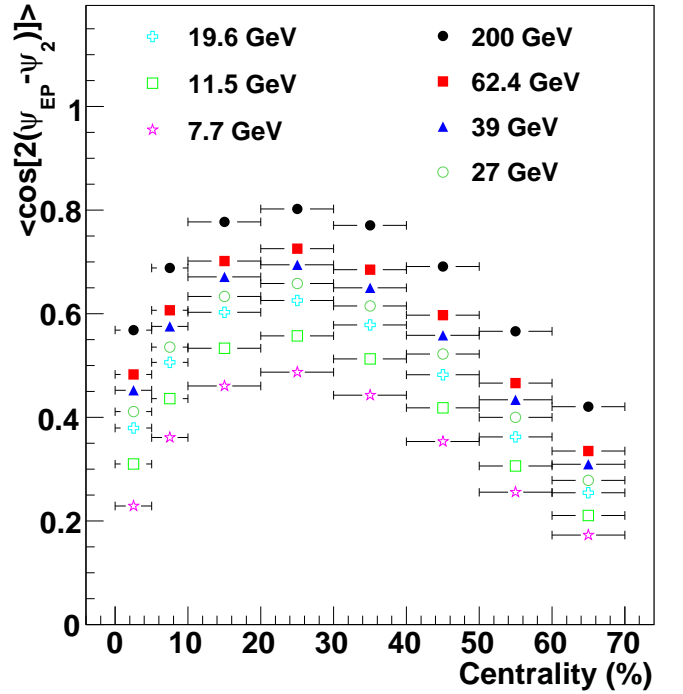

FIG. 3: (Color online) The event plane resolutions for Au+Au collisions at $\sqrt{s_{NN}}$ = 7.7, 11.5, 19.6, 27, 39, 62.4 and 200 GeV as a function of collision centrality. The resolutions, computed using the TPC ($|\eta| < 1$), enter into both the correction algorithm and the global fit method. Statistical errors are smaller than the symbols.

be computed in order to correct for this effect later in the analysis. The nth order event plane angle, ψ_n, is determined using charged particles measured in the TPC according to the equation

$$\psi_n = \frac{1}{n} \arctan\left(\frac{Q_y}{Q_x}\right) + \Delta\psi_n \qquad (4)$$

where the components of the event plane vector are

$$Q_x = \frac{1}{N} \sum_i \left(w_i \cos(n\phi_i) - \langle Q \rangle_x\right) \qquad (5)$$

$$Q_y = \frac{1}{N} \sum_i \left(w_i \sin(n\phi_i) - \langle Q \rangle_y\right). \qquad (6)$$

Here, ϕ_i is the angle of the ith track and N is the total number of tracks used to determine the event plane. The shift correction [58] is given by

$$\Delta\psi_n = \sum_{\alpha=1}^{\alpha_{max}} \frac{2}{\alpha}(-\langle \sin(n\alpha\psi_n)\rangle \cos(n\alpha\psi_n)$$
$$+ \langle \cos(n\alpha\psi_n)\rangle \sin(n\alpha\psi_n)) \qquad (7)$$

where α determines the order ($n\alpha$) that each correction term flattens. This analysis is performed relative to the second-order ($n = 2$) event plane.

For 7.7-39 GeV, the ϕ-weighting method [58–61] was used to flatten the event plane. The inverse, single particle, azimuthal distribution is used to weight each particle in the event plane determination so that inefficiencies do not affect the event plane determination. The ϕ-weight, $\phi_{\mathrm{wgt},i}$, is selected from this distribution for the ith particle using the direction of the particle's transverse momentum vector, $\vec{p}_{T,i}$. In this case $w_i = \phi_{\mathrm{wgt},i} \cdot p_{T,i}$ while the recentering terms $\langle Q \rangle_x$ and $\langle Q \rangle_y$, as well as the shift term $\Delta\psi_n$, are all zero.

For 62.4 and 200 GeV a problematic sector of the TPC was turned off causing a rather non-uniform azimuthal distribution. In this case the recentering and shift methods [58, 60, 62] were required to determine the event plane accurately. In this case, ϕ-weights were not applied so $w_i = p_{T,i}$. Here, the average offset in the direction of the p_T weighted flow vector, $\vec{Q}$, is used to compute $\langle Q \rangle_x$ and $\langle Q \rangle_y$. After this correction is applied, a shift method is needed to correct the event plane values for effects due to other harmonics. The shift term $\Delta\psi_n$ is determined by computing the correction terms $\langle \sin(n\alpha\psi_n) \rangle$ and $\langle \cos(n\alpha\psi_n) \rangle$ from $\alpha = 1$ up to $\alpha = 20$ terms, although generally $\alpha_{\max} = 2$ would be sufficient for a second order analysis [58].

The event plane resolution, $\langle \cos[2(\psi_{\mathrm{EP}} - \psi_2)] \rangle$, due to differences between the reconstructed (ψ_{EP}) and actual (ψ_2) reaction planes, is also needed as it enters the correction algorithm described later. The calculation begins by determining two event planes for two independent subevents which in this analysis correspond to the $\eta < 0$ and $\eta > 0$ regions, so called η subevents. These subevent plane estimates are processed through an iterative procedure to solve for the full event plane resolution as outlined in [58]. Resolutions are reduced for lower multiplicity (and therefore lower energy) as well as more round (less anisotropic) cases. The values at each energy that enter this specific analysis are included in Fig. 3.

E. Systematic uncertainties

The sources of systematic uncertainty have been studied in previous HBT analyses such as [33–35, 40]. Similar studies have been used to estimate the systematic uncertainty due to the Coulomb correction, fit range, and fraction of merged hits (FMH) cut discussed earlier. The azimuthal analysis is most sensitive to the fraction of merged hits requirement and this is used to estimate the systematic uncertainty. For lower energies the dependence of the fit parameters on the allowed fraction of merged hits is consistent with earlier results at $\sqrt{s_{NN}} = 200$ GeV. Reduction of the Coulomb radius from 5 fm to 3 fm and variation of the fit range from 0.15 GeV/c to 0.18 GeV/c, also leads to results similar to earlier studies. Track splitting is effectively eliminated. The uncertainties are estimated to be the same for each $\sqrt{s_{NN}}$ reported here and are summarized in Table II, for each source, for the HBT radii and freeze-out eccentricity (defined in Sec. VI B 3).

Earlier STAR analyses [33–35, 40] found, for various collision species (p+p, Cu+Cu, Au+Au) and data sets that the systematic uncertainty is approximately 10% or less for the HBT radii in all centrality and k_T bins studied. Analogous

Source	R_{out}	R_{side}	R_{long}	ε_F
Coulomb	4%	3%	4%	0.004
Fit Range	5%	5%	5%	0.002
FMH	7%	3%	3%	0.003
Total	9.5%	6.5%	7%	0.005

TABLE II: The approximate systematic uncertainty on the HBT radii and freeze-out eccentricities.

studies lead to the same conclusion for the data sets used in the current analysis and suggest the uncertainties are virtually independent of beam energy.

It should be noted that there is also an inherent uncertainty in the general method used to extract the eccentricity. The theoretical framework assumes a static, Gaussian region of homogeneity that corresponds to the entire volume of the collision at kinetic freeze-out. Flow-induced space-momentum correlations reduce this correspondence which could affect the reliability of the equations. However, several different model studies [23, 24] find consistently that the results are still reliable to within 30%, even in the presence of strong flow. This would not affect any conclusions regarding the shape of the excitation function in regards to whether or not it is monotonic.

V. EXTRACTING RADIUS OSCILLATIONS

In azimuthally differential analyses, correlation functions are constructed for pairs directed at different angles relative to the event plane. The HBT radii that describe these regions exhibit sinusoidal variations relative to the event plane direction. Second order oscillations of these radii can be described in terms of Fourier coefficients which have been related to the eccentricity of the collision fireball at kinetic freeze-out. Due to finite-bin-width and event plane resolution, the amplitude of these oscillations is reduced from the actual value. In order to determine the true amplitudes, these effects must be taken into account. Three methods of correcting for these effects will be described later in this section.

In the azimuthal HBT analysis, four correlation functions are constructed, for pairs directed in four different angular bins centered at $\Phi = 0°$, $45°$, $90°$, and $135°$ relative to event plane. This allows extraction of the second order sinusoidal variations of the HBT radii. Figure 4 shows an example of these oscillations. The Φ dependence of the HBT radii for a given beam energy, centrality, and k_T are described by:

$$R_\mu^2(\Phi) = R_{\mu,0}^2 + 2 \sum_{n=2,4,6...} R_{\mu,n}^2 \cos(n\Phi) \qquad (\mu = o,s,l,ol) \quad (8)$$
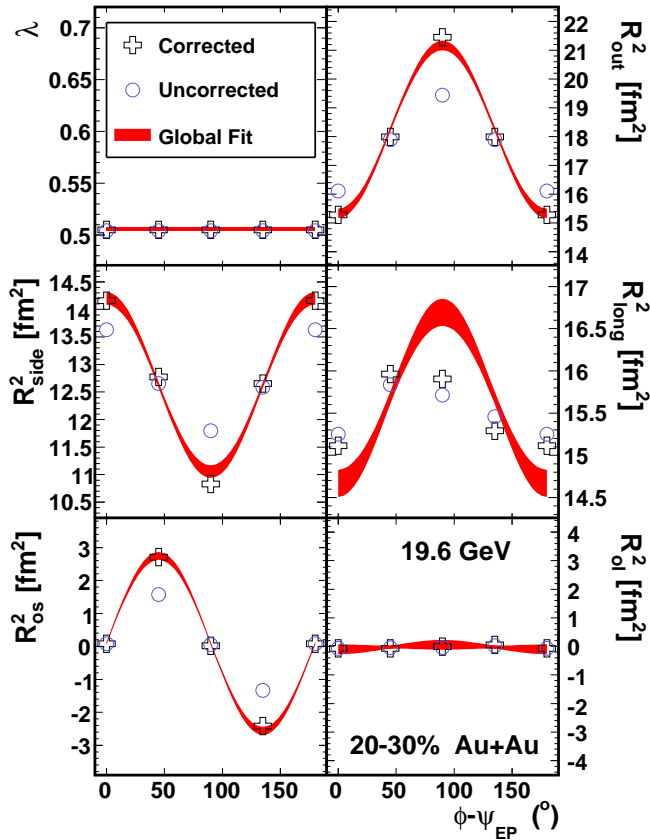
FIG. 4: (Color online) Examples of the angular oscillations of the HBT radii relative to the event plane from 20-30% central, 19.6 GeV Au+Au collisions for $0.15 < k_T < 0.6$ GeV/c. Open circles show the radii before correction for finite-bin-width and event plane resolution. Open cross symbols demonstrate that correcting these effects increases the oscillation amplitude. The corrected and uncorrected results are obtained with the HHLW fit method (see text) before and after the correction algorithm (Sec. V B) is applied. The points at $0°$ are repeated on the plot at $180°$ for clarity. The solid bands show the Fourier decomposition directly extracted using a global fit (Sec. V C) to all four angular bins; the width of the bands represent 1-sigma uncertainties from the fit. The value of λ is consistent for the two methods.

and

$$R_\mu^2(\Phi) = R_{\mu,0}^2 + 2 \sum_{n=2,4,6...} R_{\mu,n}^2 \sin(n\Phi) \qquad (\mu = os) \qquad (9)$$

where $R_{\mu,n}^2$ are the nth-order Fourier coefficients for radius term μ. These coefficients are computed using

$$R_{\mu,n}^2 = \begin{cases} \langle R_\mu^2(\Phi) \cos(n\Phi) \rangle & (\mu = o, s, l, ol) \\ \langle R_\mu^2(\Phi) \sin(n\Phi) \rangle & (\mu = os) \end{cases} \qquad (10)$$

The 0th-order Fourier coefficients are expected to be nearly identical to radii extracted in an azimuthally integrated analysis. The 2nd-order terms correspond to half the amplitude of

the second order oscillations for a second order, $n = 2$, analysis.

The extracted HBT radii display the expected [53] symmetries expressed in equations 10. The 3-σ difference between the R_{long}^2 values at $45°$ and $135°$ is eye-catching, but is statistical in nature.

Imperfect event plane resolution smears the difference between neighbouring azimuthal bins and it also causes the peaks of the extracted oscillations of the HBT radii to appear smaller than they ideally should be. These effects must be corrected for in order to extract the true 2nd-order oscillation amplitudes needed to compute the kinetic freeze-out eccentricities, ε_F, which are discussed in Sec. VI B 3. In the following discussion, two methods that have been applied in earlier analyses (which we refer to as the E895 and HHLW methods) are reviewed. A third method used in this analysis, dubbed the global fit method, is then introduced.

A. E895 method

In an earlier azimuthal HBT analysis performed by the E895 collaboration [39] and a later analysis by the CERES collaboration [42], the radii were extracted from correlation functions that were uncorrected for finite-bin-width and resolution effects. These uncorrected radii were then used to compute the Fourier coefficients described above. The uncorrected, 2nd-order Fourier coefficients were then scaled by dividing by the event plane resolution, as is done when correcting a v_2 measurement for event plane resolution effects. While this is found to give consistent results to other methods described below, it is formally incorrect because it is not the radii that are smeared, but rather each q-space bin for each of the numerator, denominator and Coulomb weighted mixed event distributions separately. This method will be referred to as the E895 method.

B. HHLW method

In this method, used first in [40], a model independent correction algorithm is applied to compute the corrected numerator, denominator, and Coulomb weighted denominator histograms for each angular bin. The radii extracted from these corrected distributions are then used to compute the Fourier coefficients. This method will be referred to as the HHLW method after the authors of the paper in which it was developed [53]. We briefly summarize this correction procedure below.

The derivation, detailed in Ref. [53], requires first decomposing mathematical expressions for the true (corrected) and experimental distributions as Fourier series. The true distributions are then convolved with a (Gaussian) distribution of the reconstructed event plane centered about the reaction plane, and a function to account for the finite azimuthal bin width. Finally, each coefficient from the series for the true distribution is equated with the corresponding coefficient from the series expansion of the experimental distribution. This leads

to the following relationship between coefficients for the true and experimentally observed distributions:

$$A_{\alpha,n}^{\text{exp}}(\vec{q}) = A_{\alpha,n}(\vec{q}) \frac{\sin(n\Delta/2)}{n\Delta/2} \langle \cos[n(\psi_{\text{EP}} - \psi_2)] \rangle. \quad (11)$$

The quantities $A_{\alpha,n}(\vec{q})$ and $A_{\alpha,n}^{\text{exp}}(\vec{q})$ are the coefficients for the Fourier series representation of the true and experimental distributions respectively. The formula applies separately to the numerator ($A=N$) and the denominator ($A=D$) of Eq. 2 and the Coulomb weighted mixed event ($A=K_{\text{Coul}}$) distributions. The factors multiplying $A_{\alpha,n}(\vec{q})$ come from the convolution of the true series mentioned previously. The quantities $\langle \cos[n(\psi_{\text{EP}} - \psi_2)] \rangle$ are the reaction plane resolutions. The symbol Δ is the width of each angular bin and n is the order of the Fourier coefficient. The experimental coefficients can be computed from the experimentally measured distributions in each angular bin using the standard definition for Fourier coefficients so that

$$A_{\alpha,n}^{\text{exp}}(\vec{q}) = \begin{cases} \langle A_n^{\text{exp}}(\vec{q}, \Phi) \cos n\Phi \rangle & (\alpha = c) \\ \langle A_n^{\text{exp}}(\vec{q}, \Phi) \sin n\Phi \rangle & (\alpha = s) \end{cases} \quad (12)$$

are the coefficients for the cosine ($\alpha = c$) or sine ($\alpha = s$) terms in the series expansion.

The corrected distributions can be computed from the experimental distributions using

$$A(\vec{q}, \Phi_j) = A^{\text{exp}}(\vec{q}, \Phi_j) + 2 \sum_{n=1}^{n_{\text{bins}}} \zeta_n(\Delta) \\ \times [A_{c,n}^{\text{exp}}(\vec{q}) \cos(n\Phi_j) + A_{s,n}^{\text{exp}}(\vec{q}) \sin(n\Phi_j)]. \quad (13)$$

In this analysis, only the 2nd-order event plane, ψ_2, is measured, and so only the $n=2$ terms are required. The correction parameter $\zeta_n(\Delta)$ is given by

$$\zeta_n(\Delta) = \frac{n\Delta/2}{\sin(n\Delta/2)\langle \cos[n(\psi_{\text{EP}} - \psi_2)] \rangle} - 1. \quad (14)$$

Substituting Eq. 14 into Eq. 13 leads to an identity, with only experimentally measured quantities on the right hand side.

Once the corrected numerator, denominator, and Coulomb weighted mixed-event distributions are computed for each angular bin, fits are performed to extract the radii. As in [40], the λ parameter from the four angular bins are averaged (for each centrality) and set as a constant for all four bins; the $\langle \lambda \rangle$ values are nearly identical to the non-azimuthal cases. The correlation functions are refit to extract the radii. The λ-fixing procedure reduces the number of independent fit parameters needed. We have checked that removing this restriction from the fits results in no significant Φ-dependence of λ, but only results in slightly larger errors for the radii, due to the increase of parameters.

In any case, the HBT radii extracted from these corrected distributions exhibit the true, larger oscillation amplitude. This is clearly demonstrated in Fig. 4. One deficiency in this approach is that the uncertainties on the corrected distributions are correlated, leading to an underestimate of the uncertainties for the extracted radii. We have developed a global fit method, described next, to avoid this issue.

C. Global fit method

A new global method of fitting was developed that avoids correlated errors and provides more reliable results in cases of low statistics and poor event plane resolution. The method begins with the same Gaussian parameterization as in Eq. 3. The Fourier representation of the radii from Eqs. 8 and 9 are substituted, keeping only the 0th- and 2nd-order terms. In this method, the fit parameters are the Fourier coefficients that describe the oscillations of the radii relative to the event plane, and so the Fourier coefficients are extracted directly rather than the radii. Using this parameterization, the theoretical estimate of the true numerator, N^{true}, is then smeared for event plane resolution and finite-binning effects by applying the correction algorithm in reverse, as described below. In this way, a theoretical estimate of the values expected in each uncorrected numerator, N^{smeared}, is obtained which can then be compared to the uncorrected numerators that are experimentally measured, N^{exp}.

For each bin $\vec{q} = (q_o, q_s, q_l)$, a value of the correlation function, $C^{\text{true}}(\vec{q})$, is computed. An estimate for the denominator is obtained from the "true" denominator, $D(\vec{q})$ (i.e., the denominator for a given Φ bin run through the correction algorithm described in the last section). The estimate for the true numerator, for each $\vec{q}$ bin, is simply $N^{\text{true}}(\vec{q}) = D(\vec{q})C^{\text{true}}(\vec{q})$. This value is then run through the correction algorithm in reverse. A series similar to Eq. 13,

$$N^{\text{smeared}}(\vec{q}, \Phi_j) = N^{\text{true}}(\vec{q}, \Phi_j) + 2 \sum_{n=1}^{n_{\text{bins}}} \zeta_n'(\Delta) \\ \times [N_{c,n}^{\text{true}}(\vec{q}) \cos(n\Phi_j) + N_{s,n}^{\text{true}}(\vec{q}) \sin(n\Phi_j)], \quad (15)$$

is used to compute the value expected to appear in the uncorrected numerator, N^{exp}, for each (q_o, q_s, q_l) bin and each Φ bin. The quantity N^{smeared} is the value expected in the uncorrected numerator, N^{exp}, based on the value, N^{true}, predicted by the current values of the fit parameters during each iteration of the fit algorithm. All fit parameters (including normalizations) obtained in this method correspond to the true correlation function even though the fit is applied to the uncorrected numerators. As in Eq. 13, only $n=2$ terms are used for an analysis relative to the second order event plane.

A factor similar to Eq. 14, from the same relationship between true and experimental values,

$$\zeta_n'(\Delta) = \frac{\sin(n\Delta/2)\langle \cos[n(\psi_{\text{EP}} - \psi_2)] \rangle}{n\Delta/2} - 1 \quad (16)$$

smears the true amplitude according to the resolution and finite-bin-width when substituted into Eq. 15.
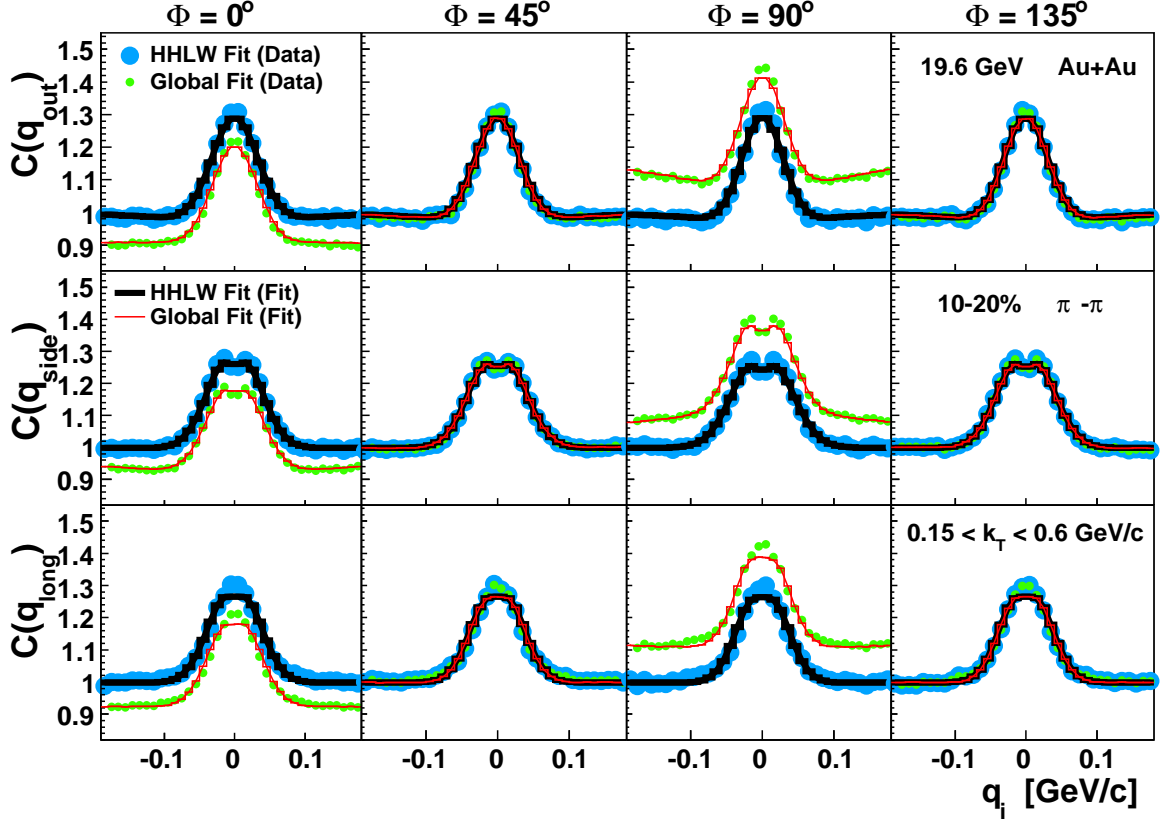
FIG. 5: (Color online) Sample fit projections onto the q_{out} (top row), q_{side} (middle row) and q_{long} (bottom row) axes for four angular bins relative to the reaction plane. Results from the HHLW fit method and the global fit method are shown for direct comparison. These projections are from results for 10-20% central, 19.6 GeV Au+Au collisions with $0.15 < k_T < 0.6$ GeV/c.

In this way, an estimate, N^{smeared}, of the value that should be found in the uncorrected, raw numerator histogram, N^{exp}, for each (q_o, q_s, q_l) bin in each Φ bin is obtained from the fit function. The value expected by the fit function is compared to the value actually observed in each (q_o, q_s, q_l) bin in the four uncorrected numerator histograms for all four Φ bins in a single simultaneous "global" fit.

A separate normalization is used for each Φ bin since there will be differences in the number of tracks, and therefore pairs, in the different bins. A single λ parameter is used for all four angular bins, as is done in the HHLW fit method. The global fit method significantly reduces the number of parameters needed to describe the data from 21 parameters (λ + 5 radii x 4 Φ bins) in the HHLW method to 11 parameters (λ + 10 Fourier coefficients), not counting the four normalization parameters.

The HHLW correction algorithm computes a corrected histogram from all of the uncorrected histograms. Therefore, the uncertainties in each corrected histogram depend on the uncertainties in all the uncorrected histograms. While the uncertainties are independent in the uncorrected histograms, the uncertainties in the "corrected" histograms are not. However, the fit assumes the uncertainties are independent and, as a result, underestimates the true uncertainty. The new method, by fitting directly to the uncorrected numerator histograms,

avoids this problem.

A disadvantage of the new algorithm is that the normalizations obtained correspond to the "true" correlation function, $C^{\text{true}}(\vec{q}) = N^{\text{true}}(\vec{q})/D^{\text{true}}(\vec{q})$, but the fit uses the corrected denominator histogram, $D(\vec{q})$, as in the HHLW method, and the uncorrected numerator histogram, $N^{\text{exp}}(\vec{q})$. To compare the fit to the distributions that are actually used in the fit, $C'(\vec{q}) = N^{\text{exp}}(\vec{q})/D(\vec{q})$ is projected onto the out, side and long axes, but the normalizations do not correspond exactly. They do put the projections on a common scale however. The 0° and 90° projections are shifted away from unity at large $\vec{q}$. Examples of the projections using the global fit method are shown in Fig. 5 for the same centrality and energy as the fits using the HHLW fit method, also shown in Fig. 5 for comparison. As a check, if instead one projects $N(\vec{q})/D(\vec{q})$ and $N^{\text{fit}}(\vec{q})/D(\vec{q})$, where $N^{\text{fit}}(\vec{q})$ is the unsmeared fit numerator computed from the extracted Fourier coefficients (from the global fit method), the projections look essentially identical to the HHLW fit method projections for all four angular bins.

For most centralities and fit parameters, the results agree quite well. However, the amplitude describing the R^2_{long} oscillation, $R^2_{l,2}$, is larger when obtained using the new fit method. This is demonstrated most clearly in Fig. 4 by comparing the solid band for the oscillation extracted using the global fit method to the corrected radii using the HHLW method. The

difference in $R^2_{l,2}$ for the two parameterizations means that the second order oscillation that best fits the data from all angular bins simultaneously is not consistent with the Gaussian R_{long} values that best describe the regions of homogeneity in each angular bin separately. While Gaussian fits are useful for characterizing overall system scales, it has been shown [33] that the correlation function at these energies is least Gaussian in the longitudinal direction. Hence, 5-10% discrepancies in R^2_{long} from different Gaussian fits is perhaps unsurprising.

The difference may be exacerbated by a subtle interdependence of the fit parameters in the HHLW fit method that constrains the R_{long} values. Also, the new fit method has difficulties in all central 0-5% cases and in a few 5-10% cases when the statistics become low. These cases are excluded, for instance, from Fig. 12 as well as all other figures for the azimuthally differential analysis. For some of the 0-5% cases the fit could never converge even with high statistics. For these unreliable cases, while the $R^2_{ol,2}$ values are close to zero in the HHLW fit results for all centralities, a large $R^2_{ol,2}$ suddenly appears in this most central bin when using this global fit method. This is likely non-physical because, for a symmetric acceptance window around mid-rapidity, R^2_{ol} must average to zero. Additionally, because the different angular bins are most similar in central events any second order oscillation of $R^2_{ol,2}$ should decrease in the most central bin due to symmetry, not appear suddenly. In fact when $R^2_{ol,2}$ is varied, the χ^2 value between the fit and the data becomes quite flat for the central data compared to other centralities allowing $R^2_{ol,2}$ to take on a wide range of values without constraint. Additionally, when this happens the oscillations extracted for some, or sometimes all, of the other parameters ($R^2_{o,2}, R^2_{s,2}, R^2_{l,2}$) change sign in this central case, even when statistics are high.

Due to the symmetry of the almost round central events, the distributions for different angular bins are quite similar compared to other centralities. The global fit method extracts oscillations, not radii, from all four bins simultaneously, and when the distributions are similar it seems to have the freedom to find a wider variety of solutions. The HHLW fit method, with separate fits in each azimuthal bin, has no such freedom, but is found to be less reliable when statistics and resolutions are low. For the global fit method, for other centralities, the results are rather stable. The 0$^{\text{th}}$-order coefficients remain consistent with the azimuthally integrated results, which is even true for 0-5% centrality. The behavior for central data appears to be the result of the relationship between the fit parameters used, the similar shape of the emission regions for all the angular bins in the central data, and the very shallow minimum in χ^2 that develops for $R^2_{ol,2}$ at the same time. There are no other differences in the global fit algorithm compared to the HHLW fit method.

VI. RESULTS

The azimuthally integrated HBT results are discussed first and compared to historical data from earlier experiments and recent results from ALICE. Later, the azimuthally differential analysis is presented for a wide range of beam energies. The azimuthally differential analysis is also performed in three rapidity bins allowing extraction of the excitation function for the R^2_{ol} parameter and direct comparison of the freeze-out eccentricity in the same forward rapidity window as an earlier measurement by the CERES collaboration. Finally, the excitation function for the freeze-out eccentricity is discussed along with its implications for the relevant underlying physics as outlined in Sec. II.

A. Azimuthally integrated HBT

There is a wealth of earlier HBT data demonstrating the systematic behavior of the HBT radii as a function of beam energy, k_T (or m_T), and centrality. Trends have been established despite the measurements having been performed by various experiments and with differences in the analysis techniques. In this paper, the results are presented across a wide range of beam energies, overlapping previously measured regions and filling in previously unmeasured regions of $\sqrt{s_{NN}}$.

Figure 6 shows the beam energy dependence of the λ parameter, the HBT radii, and the ratio $R_{\text{out}}/R_{\text{side}}$ for like-sign pions in central collisions at low k_T. All the STAR results are from the most central 0-5% and lowest $\langle k_T \rangle$ (≈ 0.22 GeV/c) data. The ALICE point is also from 0-5% central data, but has a slightly larger $\langle k_T \rangle \approx 0.26$ GeV/c. Results from earlier experiments come from a range of central data sets, as narrow as 0-7.2% to as wide as 0-18% centrality, as well as a range of $\langle k_T \rangle$ values, from 0.17 GeV/c to 0.25 GeV/c. The earlier data are from π^--π^- correlation results in which various methods of accounting for the Coulomb interaction were employed. The new STAR results are from combined π^--π^- and π^+-π^+ correlation functions. No significant difference between the two cases has been observed so the combination simply leads to higher statistics. Our high-statistics analysis, with identical acceptance for all $\sqrt{s_{NN}}$, yields a well-defined smooth excitation function consistent with the previous trends.

The λ parameter primarily represents the fraction of correlated pairs entering the analysis, as described in Sec. IV B. It decreases with increasing $\sqrt{s_{NN}}$ relatively rapidly at lower, AGS, energies while changing rather little from 7.7 to 200 GeV. This suggests that the fraction of pions in this $\langle k_T \rangle$ range from long-lived resonances increases at lower energy but remains rather constant at higher energies. The value of λ is larger than our earlier reported results for 200 GeV [33] which is related to our implementation of an anti-electron cut that reduces contamination in this analysis. The R_{out} parameter similarly shows little change over a wide range of RHIC energies. It does appear to rise noticeably at the LHC. The values of R_{side} show a very small increase at the higher RHIC energies and a more significant increase at the LHC. The values of R_{long}, on the other hand, appear to reach a minimum around 5 GeV, rising significantly at RHIC and the ALICE point is once again higher than the trend observed at STAR.

The radius R_{side} is primarily associated with the spatial extent of the particle emitting region, whereas R_{out} is also affected by dynamics [23, 24] and is believed to be related to the duration of particle emission [63, 64].
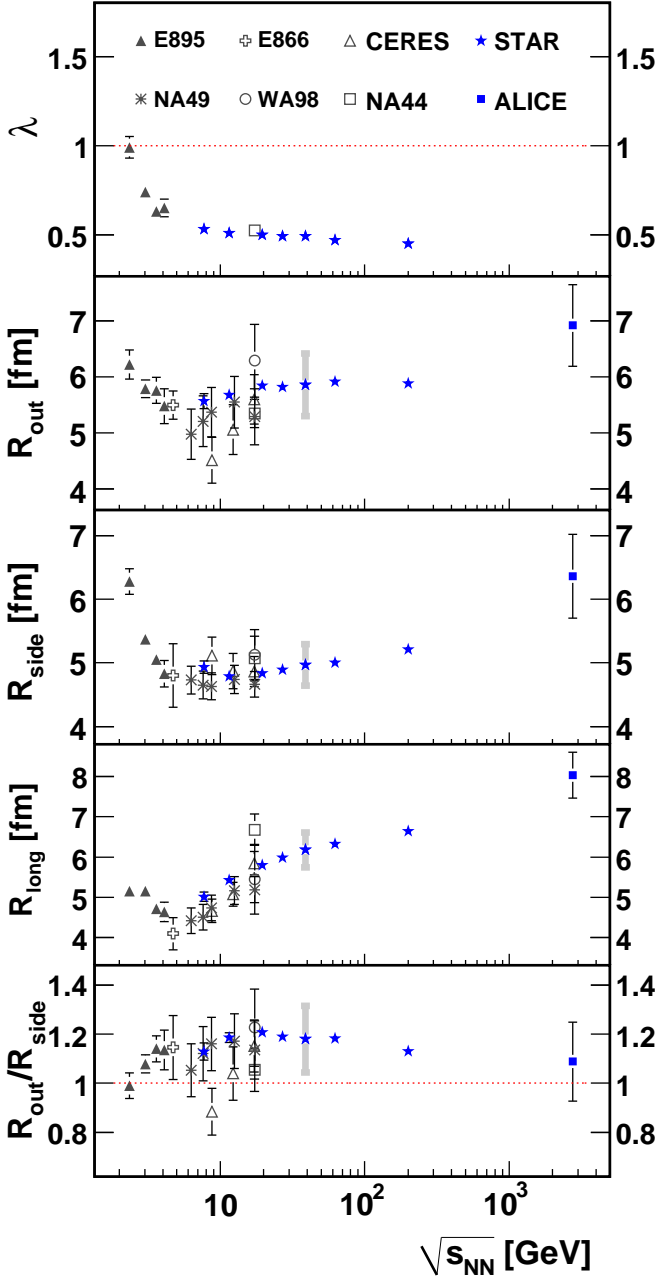
FIG. 6: (Color online) Energy dependence of the HBT parameters for central Au+Au, Pb+Pb, and Pb+Au collisions at mid-rapidity and $\langle k_T \rangle \approx 0.22$ GeV/c [26–31, 36]. The text contains discussion about variations in centrality, k_T, and analysis techniques between experiments. Errors on NA44, NA49, WA98, CERES, and ALICE points include systematic errors. The systematic errors for STAR points at all energies (from Table II) are of similar size to error bar for 39 GeV, shown as a representative example. Errors on other results are statistical only, to emphasize the trend. For some experiments the λ value was not specified.

FIG. 7: Top panel: The difference between the squared transverse HBT radii are plotted as a function of the collision energy for STAR and ALICE measurements of the most central heavy ion collisions. Bottom panel: The ratio of the out and side HBT radii for STAR and ALICE are plotted for the same collisions.

In both cases, statistical errors are shown by solid error bars. Systematic errors are shown only for the data at $m_T = 0.33$ GeV ($m_T = 0.38$ GeV) for STAR (ALICE); systematic errors are common for all m_T cuts. The systematic errors are driven by two-track cuts that are common to all STAR energies and so are drawn only for the $\sqrt{s_{NN}} = 62.4$ GeV data.

It has long been suggested [50, 51, 63] that a long particle-emission duration could result in R_{out} becoming much larger than R_{side}. In the simplest scenario of a static, non-flowing

source, the emission time is given by [84]

$$(\beta \Delta \tau_{\text{static}}) = R_{\text{out}}^2 - R_{\text{side}}^2, \qquad (17)$$

where $\beta = \frac{k_T}{m_T}$ is the speed of one of the pions in the source rest frame. For a flowing source such as those created at RHIC, however, equation 17 is unreliable [22] as the dimensions of the homogeneity region probed by low-q pion pairs is affected differently in the out and side directions. Indeed, for some sources R_{out} may be smaller than R_{side} [23], in which case equation 17 would yield imaginary emission times.

It is interesting to note that the excitation function of this quantity shows a clear peak at $\sqrt{s_{NN}} \approx 20$ GeV, as seen in the top panel of figure 7. Clearly, equation 17 cannot be used, since $R^2_{out} - R^2_{side}$ becomes smaller as β increases and even becomes negative at higher $\sqrt{s_{NN}}$ and m_T. Extracing timescales from the quantity $R^2_{out} - R^2_{side}$ is necessarily model-dependent.

Prompted by Rischke and Gyulassy [63], the ratio R_{out}/R_{side} is frequently studied [22]. This ratio has the advantage of removing the overall scale of the system. Since R_{out} and R_{side} are both reduced by flow [23, 67], their ratio is slightly more robust against flow effects. The ratio is also somewhat more natural to calculate in ideal (zero viscosity) hydrodynamic theory which has no intrinsic scale. Finally, extracting radii from dynamical model calculations depends on the algorithm used [22]. Calculations that rely strictly on freezeout distributions and bypass calculation of the momentum-space correlation function, often yield HBT radii that are much too large, whereas the ratios between them are closer to experimental values. [22, 85]

In the hydrodynamic calculation of Rischke and Gyulassy, which included flow, R_{out}/R_{side} exhibited a peak as the energy density of the system nears the threshold of a first-order phase transition or rapid crossover transition [63]. This ratio is shown in the bottom panel of figure 6 for the world's dataset. A small peaking behavior in the STAR data is obscured by the historical SPS and AGS data. The excitation function is clearer if the STAR and ALICE data are viewed separately, as seen in the bottom panel of figure 7.[86] For all m_T ranges, the ratio peaks at $\sqrt{s_{NN}} \approx 20$ GeV.

It is not unreasonable to examine the RHIC and LHC data on their own. Femtoscopic techniques, including various methods for accounting for the Coulomb repulsion between the pions, have evolved over time [22]; STAR and ALICE use the Bowler-Sinyukov formalism [54, 55], which affects particularly the outward radius [33]. Furthermore, the detector acceptance and two-track efficiency change as a function of collision energy in a fixed-target experiment, which can complicate detection of a subtle trend in an observable with $\sqrt{s_{NN}}$. Mid-rapidity measurement with collider experiments such as STAR and ALICE are performed with uniform coverage independent of collision energy. Finally, systematic errors vary from one experiment to another. While the systematic error on R_{out}/R_{side} (shown as a grey band in figure 7) is significant, it is common for all $\sqrt{s_{NN}}$, so the peak in the ratio is statistically significant.

The peak in $R^2_{out} - R^2_{side}$ and R_{out}/R_{side} is intriguing, especially since it occurs around a collision energy where several other observables [87–90] show non-trivial trends that may indicate a change in the underlying physics at these energies. However, conclusive interpretation of the femtoscopic data
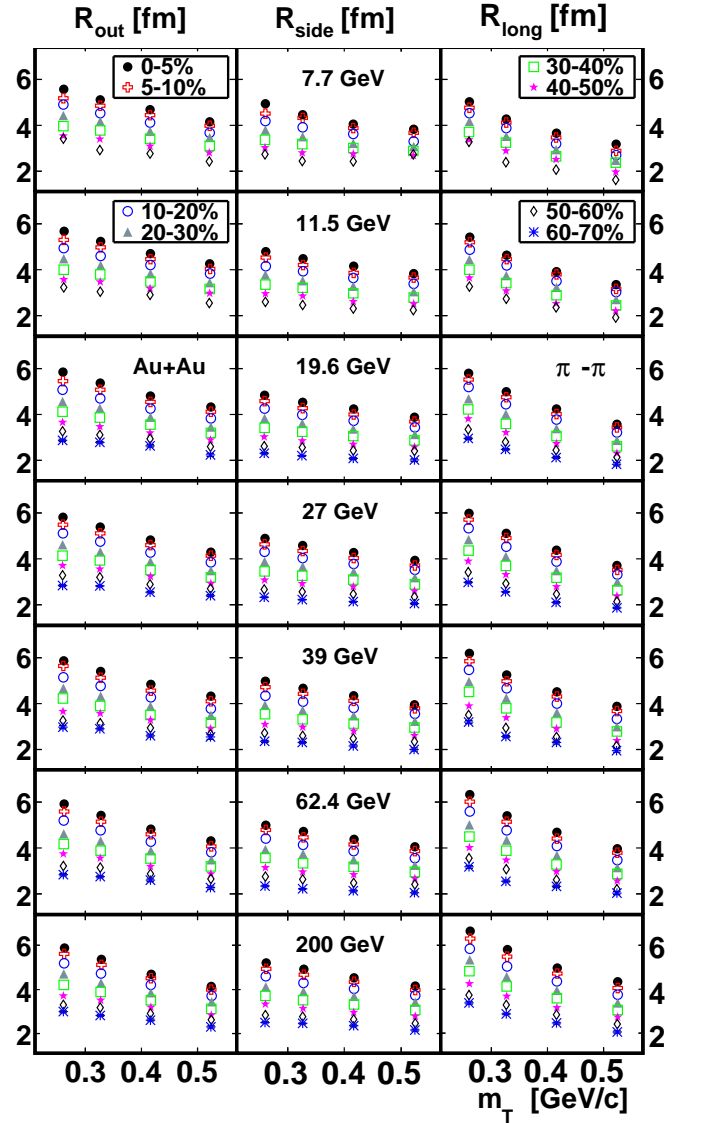

FIG. 8: (Color online) The $\langle m_T \rangle$ dependence of R_{out}, R_{side} and R_{long} for each energy and multiple centralities. Errors are statistical only. For 7.7 GeV and 11.5 GeV, the results for 60-70% centrality are excluded due to lack of statistics.

presented here must await comparison with theoretical calculations.

The value of R_{long} has been related to the kinetic freeze-out temperature, T, and lifetime, τ, of the system by the relation [23, 65, 66]

$$R_{long} = \tau \sqrt{\frac{T}{m_T} \frac{K_2(m_T/T)}{K_1(m_T/T)}} \qquad (18)$$

where $K_1(m_T/T)$ and $K_2(m_T/T)$ are modified Bessel functions. The kinetic freeze-out temperature is not expected to change much with $\sqrt{s_{NN}}$. Therefore, the rise of R_{long} suggests that the total lifetime of the system is increasing with energy. At the end of this section Eq. 18 will be used to extract τ as a
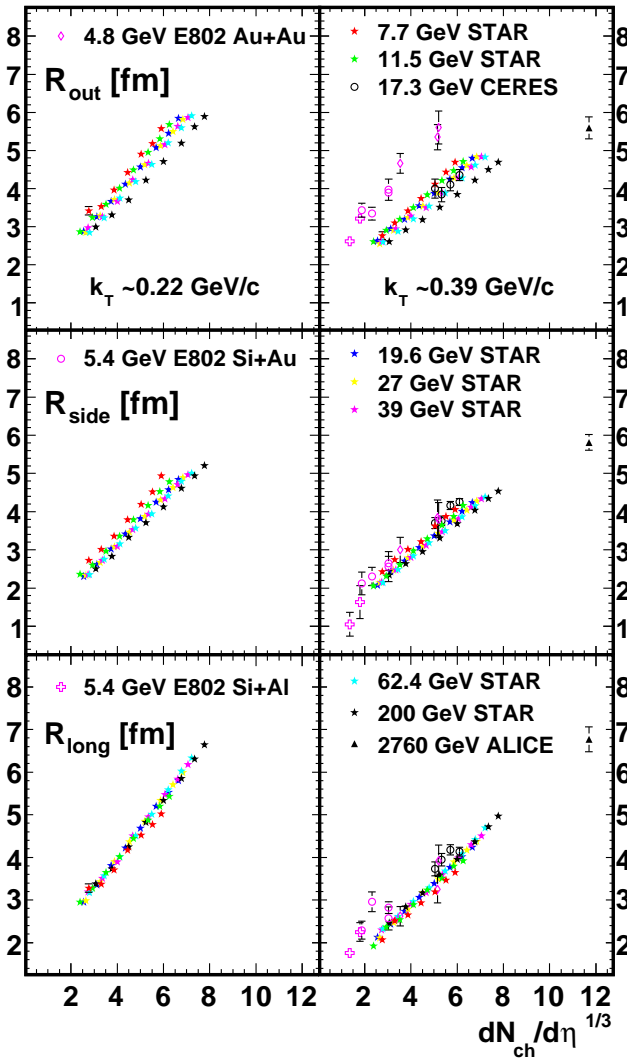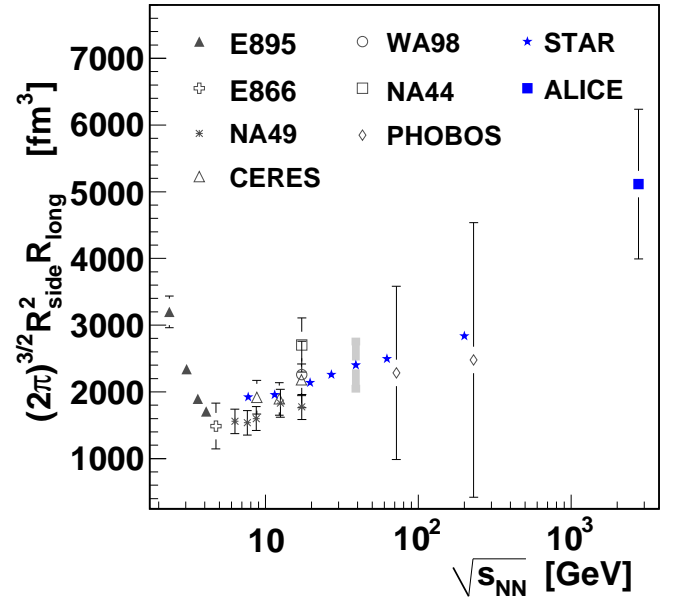
FIG. 10: (Color online) The beam energy dependence of the volume, $V = (2\pi)^{3/2}R_{side}^2 R_{long}$, of the regions of homogeneity at kinetic freeze-out in central Au+Au, Pb+Pb and Pb+Au collisions with $\langle k_T \rangle \approx 0.22$ GeV/c [26–32, 36]. The systematic errors for STAR points at all energies (from Table II) are of similar size to error bar for 39 GeV, shown as a representative example. Errors on other results are statistical only, to emphasize the trend. The PHOBOS points are offset in $\sqrt{s_{NN}}$ for clarity. The text contains some discussion about variations in centrality, $\langle k_T \rangle$, and analysis techniques between different experiments.

FIG. 9: (Color online) The dependence of the HBT radii on multiplicity, $\langle dN_{ch}/d\eta \rangle^{1/3}$, for $\langle k_T \rangle \approx 0.22$ GeV/c (left) and $\langle k_T \rangle \approx 0.39$ GeV/c (right). Results are for Au+Au collisions at STAR, Pb+Au at CERES [28], Pb+Pb at ALICE [36], and Si+A at E802 [25]. Errors are statistical only.

function of $\sqrt{s_{NN}}$ given certain assumptions.

The systematic errors for STAR points at all energies (from Table II) are of similar size to error bar for 39 GeV, shown as a representative example. Errors on other results are statistical only to emphasize the trend.

Figure 8 shows the $\langle m_T \rangle$ dependence of the HBT parameters for each energy. As mentioned earlier, the decrease in transverse and longitudinal radii at higher m_T are attributed to transverse and longitudinal flow [23, 67]. Larger m_T pairs are emitted from smaller emission regions with less correspondence to the size of the entire fireball. For both R_{out} and R_{side} the different beam energies show similar trends both in magnitude and slope. For R_{long}, the slopes appear to remain similar for the different energies, but the magnitude of R_{long} increases with energy for all centralities. From these observations, and

considering Fig. 6 showed the beam energy dependence for a single k_T and centrality bin, it is apparent that similar dependencies on $\sqrt{s_{NN}}$ exist for all the studied centrality and k_T ranges.

The multiplicity dependence of the HBT radii are presented in Fig. 9 for two k_T ranges with $\langle k_T \rangle \approx 0.22$ GeV/c and $\langle k_T \rangle \approx 0.39$ GeV/c. A few earlier measurements with similar $\langle k_T \rangle$ are shown as well. It was observed in [34] that R_{side} and R_{long} both follow a common universal trend at 62.4 and 200 GeV independent of the collision species. ALICE has recently shown p+p collisions exhibit a different multiplicity dependence with a smaller slope [37, 38]. The difference may be due to the interactions in the bulk medium formed in heavy ion collisions.

The results from ALICE are at different $\langle k_T \rangle$ values. To get a similar $\langle k_T \rangle \approx 0.39$ GeV/c estimate, the ALICE data points [36] reported for $\langle k_T \rangle \approx 0.35$ GeV/c and $\langle k_T \rangle \approx 0.44$ GeV/c are averaged and plotted on Fig. 9. There is some ambiguity in this approach as the different pair statistics at different k_T are not accounted for when averaging this way. As demonstrated in [36–38], the universal trends for R_{side} and R_{long} continue up to LHC energies.

When comparing different datasets from previous analyses [25, 28, 36], there is an uncertainty on the centrality caused by the different techniques that were used to compute the average charged track multiplicity $\langle dN_{ch}/d\eta \rangle$. In this analysis, the

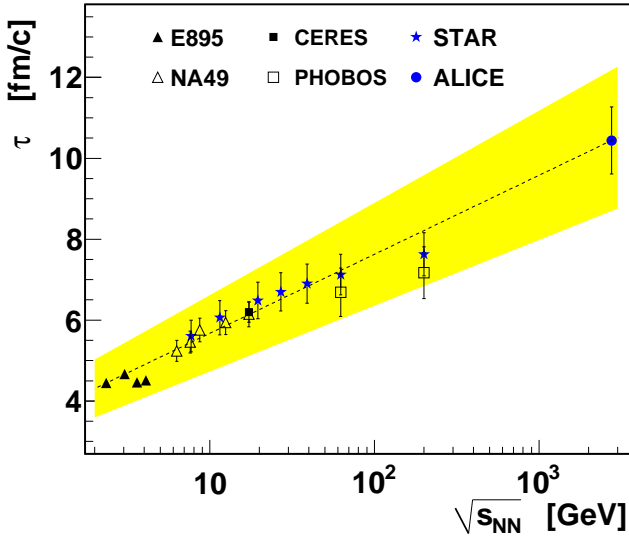FIG. 11: (Color online) The lifetime, τ, of the system as a function of beam energy for central Au+Au collisions assuming a temperature of $T = 0.12$ GeV at kinetic freeze-out. Statistical uncertainties from the fits are smaller than the data points. For all experiments except E895, which did not report systematic uncertainties, errorbars indicate systematic uncertainties, based on reported systematic uncertainty on R_{long}. The line extrapolates between the lowest and highest energy. The text contains a discussion about variations in centrality and analysis techniques between different experiments. The yellow band demonstrates the effect on τ of varying the assumed temperature by ± 0.02 GeV.

standard STAR centrality definition was used at all energies, where $\langle dN_{\text{ch}}/d\eta \rangle$ is computed using all events that pass the event selection cuts. However, it should be noted that this is an uncorrected value of $\langle dN_{\text{ch}}/d\eta \rangle$ that underestimates the true value, thus allowing for a qualitative comparison only with other experiments.

An estimate of the volume of the homogeneity regions, $V = (2\pi)^{3/2} R_{\text{side}}^2 R_{\text{long}}$, can be computed using the data in Fig. 6. These values are plotted in Fig. 10 as a function of $\sqrt{s_{NN}}$. The STAR results are all for 0-5% central collisions with $\langle k_T \rangle \approx 0.22$ GeV/c. Since the values are computed using the data in Fig. 6, all the same variations in centrality ranges and $\langle k_T \rangle$ values are present in the volume estimates too. Earlier results from other experiments suggest a minimum between AGS and SPS energies. The STAR results show a noticeable increase in volume at the higher energies while the 7.7 and 11.5 GeV points are almost the same, consistent with a minimum in the vicinity of 7.7 GeV. The ALICE point rises even further suggesting the regions of homogeneity are significantly larger in collisions at the LHC.

The CERES collaboration [68] has found that a constant mean free path at freeze-out,

$$\lambda_F \approx \frac{V}{(N_\pi \sigma_{\pi\pi} + N_N \sigma_{\pi N})} \approx 1 fm, \qquad (19)$$

leads naturally to a minimum in the energy dependence of the volume that is observed, assuming that the cross sections $\sigma_{\pi\pi}$

and $\sigma_{\pi N}$ depend weakly on energy, since the yields of pions and nucleons, N_π and N_N, change with energy. Above 19.6 GeV, the ratio of $N_\pi \sigma_{\pi\pi}/N_N \sigma_{\pi N}$ remains rather constant and the denominator in Eq. 19 increases with energy similar to the volume. Below 11.5 GeV, the $N_N \sigma_{\pi N}$ term becomes the dominant term and it increases at lower energies as does the volume. At higher energies, this scenario is consistent with the nearly universal trend of the volume on $\langle dN_{\text{ch}}/d\eta \rangle$ and, therefore, R_{side} and R_{long} on $\langle dN_{\text{ch}}/d\eta \rangle^{1/3}$ [34]. It is interesting that the multiplicity dependence for R_{side} begins to deviate slightly from this trend for 7.7 and 11.5 GeV in Fig. 9 which is the same region where the system changes from π-N to π-π dominant. Also, the argument above neglects the influence from less abundant species including kaons, but it has been observed that strangeness enhancement occurs in this same region of $\sqrt{s_{NN}}$ [69].

Another change that occurs in this region is the rapid increase of v_2 around $\sqrt{s_{NN}} = 2$-7 GeV. In the region around 7.7 to 11.5 GeV, the slope of $v_2 \left(\sqrt{s_{NN}} \right)$ begins to level off [70, 71]. A possibility is that the deviation of R_{side} for 7.7 and 11.5 GeV is related to the onset of flow induced space-momentum correlations. The E802 results at 4.8 and 5.4 GeV in the right column of Fig. 9 are qualitatively similar to the STAR 7.7 GeV results for R_{side}, but considering the STAR $\langle dN_{\text{ch}}/d\eta \rangle^{1/3}$ values are slightly underestimated, the E802 results probably deviate slightly more relative to the higher energies than even the 7.7 GeV data. For R_{out}, on the other hand, the E802 results are significantly larger than the STAR 7.7 GeV points. This could be consistent with the effects of flow. Transverse flow should reduce the size of the regions of homogeneity and is expected to affect R_{out} much more than R_{side}. This was reflected already in the larger slope for the $\langle m_T \rangle$ dependence of R_{out} relative to R_{side} in Fig. 8. It would be interesting to study these trends at lower energies with a single detector where many interesting physical changes are occuring simultaneously.

An alternative explanation of the minimum observed in the volume measurement in Fig. 10 is provided by Ultra-relativistic Quantum Molecular Dynamics (UrQMD) calculations. In [72], UrQMD also finds a minimum between AGS and SPS energies but, in this case, the cause is related to a different type of change in the particle production mechanism. At the lowest energies pions are produced by resonances, but as the energy increases more pions are produced by color string fragmentation (accounting for color degrees of freedom) which freeze-out at an earlier, smaller stage (thus a smaller volume is measured). At even higher energies, the large increase in pion yields cause the volume to increase once more. This explanation suggests that a change from hadronic to partonic degrees of freedom cause the minimum in the volume measurement. Allowing a mean field potential to act on these pre-formed hadrons (the color string fragments) leads UrQMD to predict $R_{\text{out}}/R_{\text{side}}$ values near the observed values (≈ 1) for the whole energy range from AGS to SPS [73]. Simultaneously, inclusion of the mean field for pre-formed hadrons causes UrQMD to reproduce the net proton rapidity distribution and slightly improves its prediction for $v_2(p_T)$ at intermediate p_T.
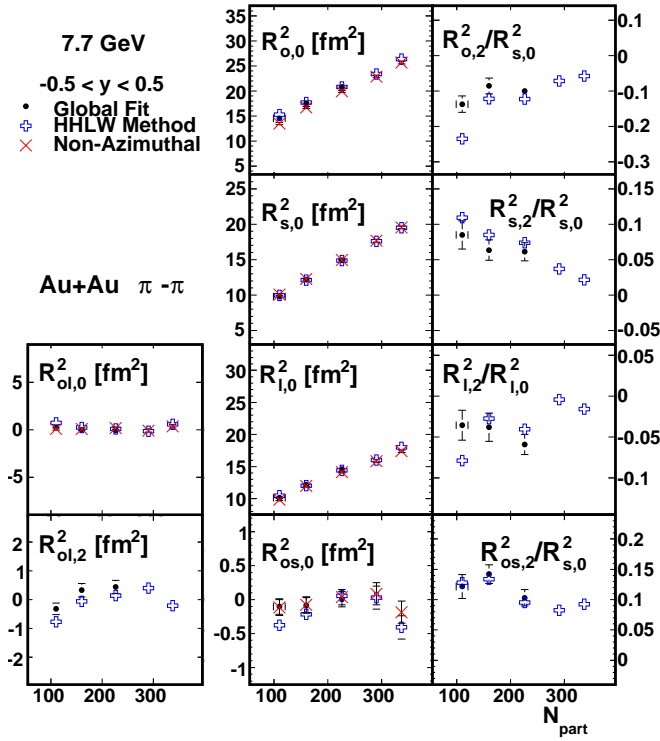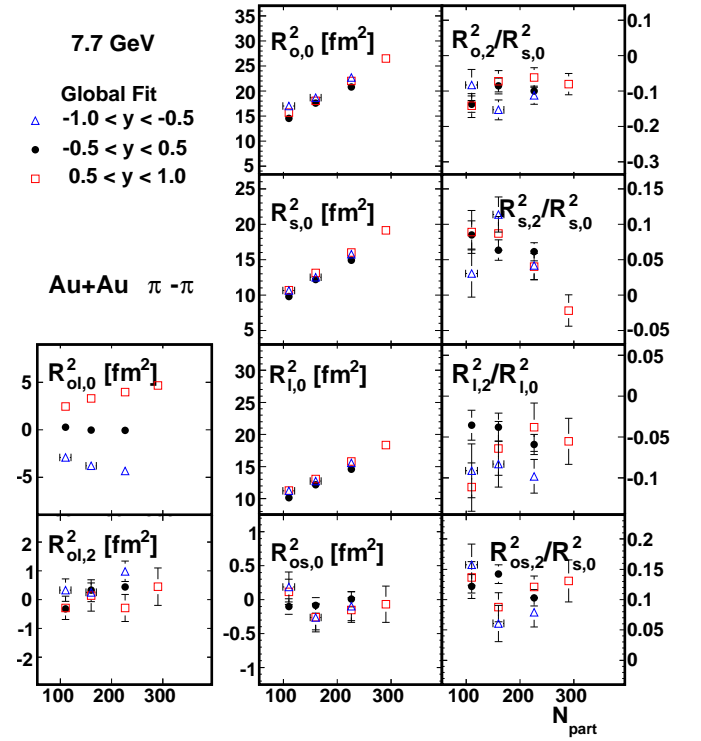
FIG. 12: (Color online) Centrality dependence of the Fourier coefficients that describe azimuthal oscillations of the HBT radii, at mid-rapidity ($-0.5 < y < 0.5$), in 7.7 GeV collisions with $\langle k_T \rangle \approx$ 0.31 GeV/c. Open symbols are results using separate Gaussian fits to each angular bin, the HHLW method. Solid circles represent results using a single global fit to all angular bins to directly extract the Fourier coefficients. Crosses directly compare the azimuthally integrated radii and the 0$^{\text{th}}$-order Fourier coefficients. Error bars include only statistical uncertainties. The 0-5% and 5-10% global fit points have been excluded.

As one last application of the data, the lifetime of the collisions is extracted in a study analogous to Ref. [36]. We also assume a kinetic freeze-out temperature of $T = 0.12$ GeV and fit the data in Fig. 8 using Eq. 18. The results are plotted in Fig. 11. The STAR results are all for 0-5% collisions with $\langle k_T \rangle \approx 0.22$ GeV/c. Again, there are some variations in the centrality ranges, as in Fig. 6, for the historical data. The extracted lifetime appears to increase from around 4.5 fm/c at the lowest energies to around 7.5 fm/c at 200 GeV, an increase of an approximate factor of 1.7. The ALICE point suggests a much longer lived system, above the trend observed at lower energies. Varying the temperature assumed in the fits to $T = 0.10$ GeV to $T = 0.14$ GeV causes the lifetimes to increase by 13% and decrease by 10%, respectively, for all energies, as indicated by the yellow band. As noted in [36], due to effects from non-zero transverse flow and chemical potential for pions, the use of Eq. 18 may significantly underestimate the actual lifetimes.

FIG. 13: (Color online) Centrality dependence of the Fourier coefficients that describe azimuthal oscillations of the HBT radii, at backward ($-1 < y < -0.5$), forward ($0.5 < y < 1$) and mid ($-0.5 < y <$ 0.5) rapidity, in 7.7 GeV collisions with $\langle k_T \rangle \approx 0.31$ GeV/c using the global fit method. Error bars include only statistical uncertainties. The 0-5% and two 5-10% points have been excluded.

B. Azimuthally differential HBT

The detailed results of the azimuthally differential analysis are presented in Figs. 12 through 27. Earlier, Fig. 4 presented an example of the second order oscillations of the HBT radii relative to the event plane for a single energy, centrality, and rapidity. These second order oscillations are represented by 0$^{\text{th}}$- and 2$^{\text{nd}}$-order Fourier coefficients, as described in Sec. V A. The Fourier coefficients are presented as a function of N_{part} in two figures for each energy, starting with Figs. 12 and 13 for 7.7 GeV and continuing through Figs. 24 and 25 for 200 GeV. For each energy, the first figure compares mid-rapidity results from the HHLW and global fit methods while the second compares forward, backward, and mid-rapidity results obtained using the global fit method. Each set of Fourier coefficients for a given N_{part} (centrality), rapidity, and energy encodes all the information for oscillations similar to those in Fig. 4.

In each of the figures showing the Fourier coefficients, the 0$^{\text{th}}$-order coefficients are presented in the middle column, for the squared radii in the out, side and long directions ($R^2_{o,0}$, $R^2_{s,0}$, $R^2_{l,0}$) and the out-side cross term ($R^2_{os,0}$). These values are expected to correspond to radii from the azimuthally integrated analysis. This correspondence is demonstrated in the first Fourier coefficient figure for each energy which also in-
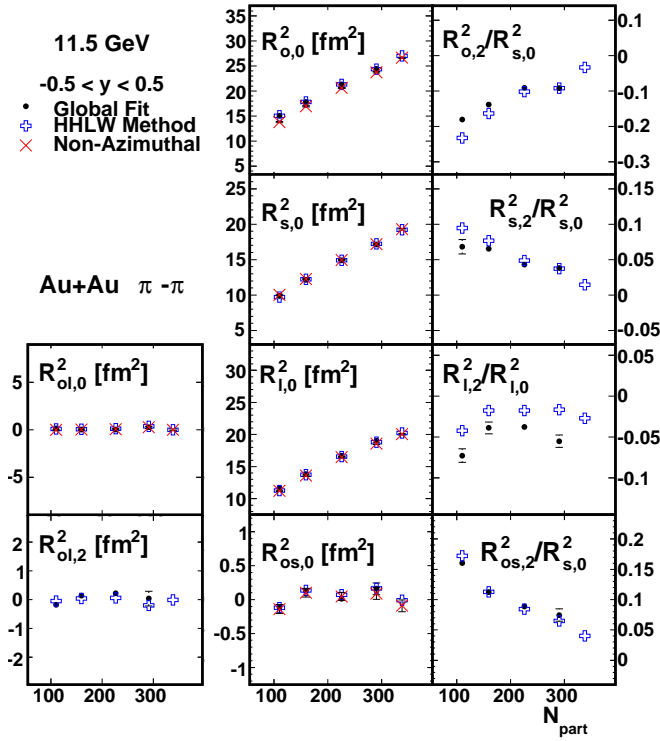
FIG. 14: (Color online) Centrality dependence of the Fourier coefficients that describe azimuthal oscillations of the HBT radii, at midrapidity ($-0.5 < y < 0.5$), in 11.5 GeV collisions with $\langle k_T \rangle \approx 0.31$ GeV/c. The symbols have the same meaning as in Fig. 12. Error bars include only statistical uncertainties. The 0-5% global fit point is excluded.
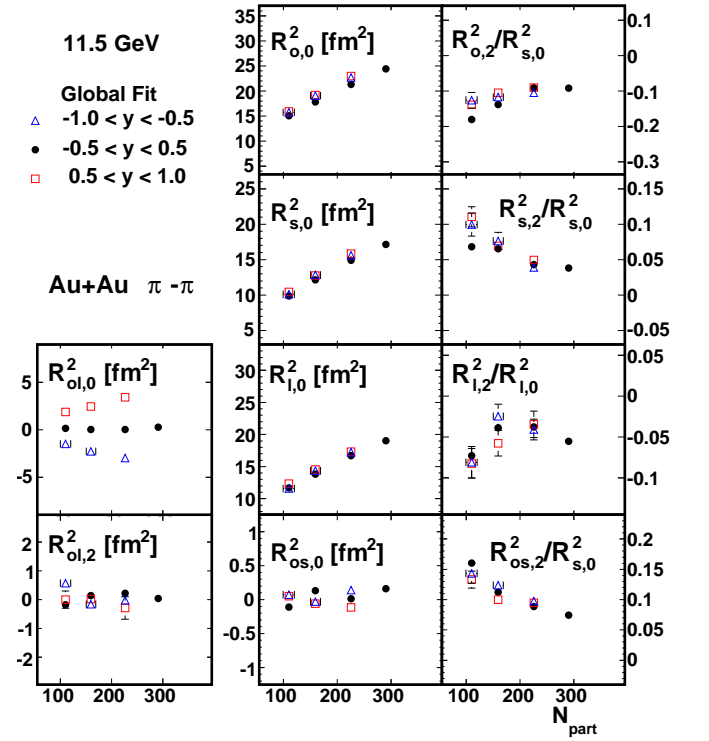
FIG. 15: (Color online) Centrality dependence of the Fourier coefficients that describe azimuthal oscillations of the HBT radii, at backward ($-1 < y < -0.5$), forward ($0.5 < y < 1$) and mid ($-0.5 < y < 0.5$) rapidity, in 11.5 GeV collisions with $\langle k_T \rangle \approx 0.31$ GeV/c using the global fit method. Error bars include only statistical uncertainties. The 0-5% and two 5-10% points have been excluded.

cludes the azimuthally integrated results (red crosses) for direct comparison. As in the azimuthally integrated case, the diagonal radii increase with centrality while the $R_{os,0}^2$ cross term remains about zero for all centralities. In the right column of these figures, ratios of 2nd-order to 0th-order coefficients are presented, also for the out, side, long and out-side parameters. The ratios that are presented have been connected to the freeze-out geometry, especially for the $R_{s,2}^2/R_{s,0}^2$ case. The left column of each of the figures contains the parameters for the out-long cross term. The 0th-order values, $R_{ol,0}^2$, are non-zero away from mid-rapidity and show interesting dependence on energy and centrality that will be discussed later.

1. Comparison of fit methods

This section provides a comparison of the HHLW fit method and the global fit method used in the azimuthally differential analysis at mid-rapidity. The first Fourier coefficient figure for each energy is relevant for this discussion. For Sec. VI B 2, the second Fourier coefficient figure for each energy is relevant for the discussion of centrality and rapidity dependence of the Fourier coefficients.

The results using the two fit methods are generally consistent for most of the parameters. For each energy, the first figure compares the Fourier coefficients from the two fit methods

at mid-rapidity. Forward and backward rapidity results are not included as some of the results become unreliable in a few cases. The reason is that at the lowest energies statistics limits the reliability, of the HHLW fit method, especially for 7.7 GeV which has the fewest events and the lowest multiplicity per event. The forward and backward rapidity regions have even lower statistics due to the narrower window of rapidity, $\Delta y = 0.5$ rather than $\Delta y = 1$. As seen in Fig. 3, the event plane resolutions are much lower at these energies as well which can amplify noise in the correlation function when the correction algorithm is applied. The correction algorithm does not distinguish between a real signal and a statistical variation. The amplitude of the variations is increased in either case. The global fit method was designed to minimize this problem by only applying the correction algorithm to the denominator which has an order of magnitude higher statistics than the numerator.

The 0th-order Fourier coefficients are expected to be consistent with the radii in the azimuthally integrated analysis. Therefore, the 0th-order, squared radii should increase smoothly with N_{part} (as in the middle column of Figs. 12 through 25). For the 0th-order terms good agreement with the azimuthally integrated results is observed for both the HHLW and global fit methods, except a few cases at the lowest energies. Especially for 7.7 GeV, with the HHLW fit method, several points, primarily the most peripheral and more cen-
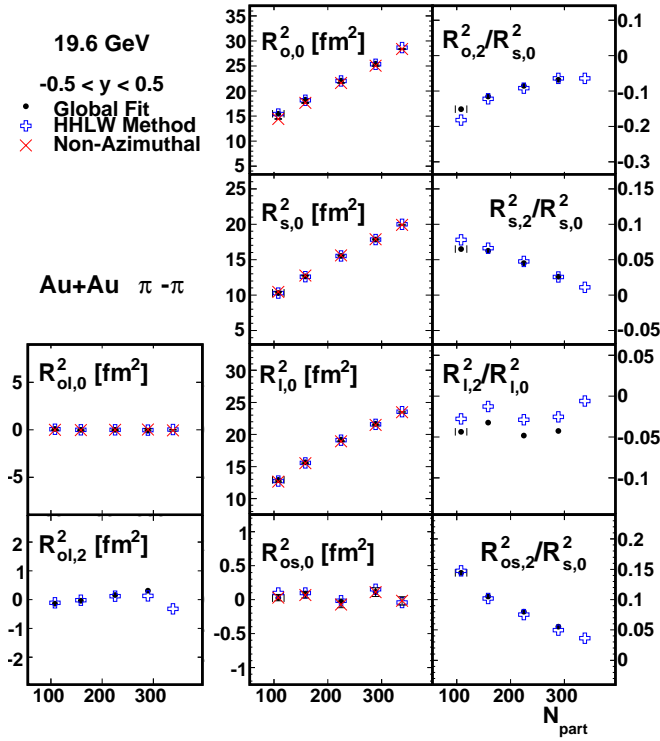
FIG. 16: (Color online) Centrality dependence of the Fourier coefficients that describe azimuthal oscillations of the HBT radii, at mid-rapidity ($-0.5 < y < 0.5$), in 19.6 GeV collisions with $\langle k_T \rangle \approx 0.31$ GeV/c. The symbols have the same meaning as in Fig. 12. Error bars include only statistical uncertainties. The 0-5% global fit point is excluded.
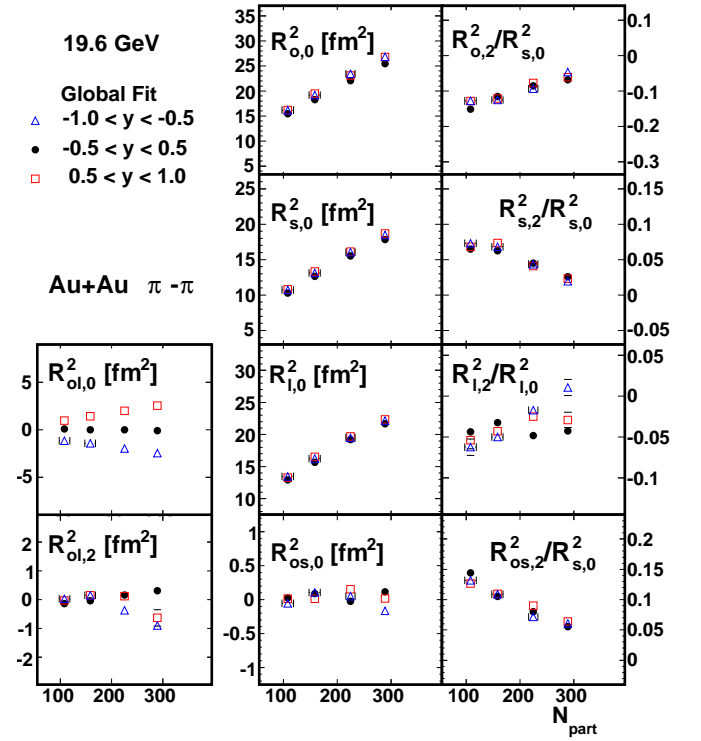
FIG. 17: (Color online) Centrality dependence of the Fourier coefficients that describe azimuthal oscillations of the HBT radii, at backward ($-1 < y < -0.5$), forward ($0.5 < y < 1$) and mid ($-0.5 < y < 0.5$) rapidity, in 19.6 GeV collisions with $\langle k_T \rangle \approx 0.31$ GeV/c using the global fit method. Error bars include only statistical uncertainties. The 0-5% global fit point is excluded.

tral (lowest statistics and resolution) points, were found to deviate quite significantly from this trend. All of these points are excluded in the figures since they are unreliable. In the same cases, however, the global fit method remains consistent with the non-azimuthal radii. Projections of the fits on the out, side, and long axes show the HHLW fit method results do not match well with the data in such cases. In particular, the 90° bin suffers most from low statistics (fewer tracks are directed out of the reaction plane) which affects both the 0th- and 2nd-order coefficients when each bin is fit separately. The global fit method results are somewhat more reliable in these low statistics and low resolution cases.

As noted earlier, there is a difference in the oscillation amplitude for the long direction, $R_{l,2}^2$, obtained from the two methods. This is shown clearly in Fig. 4 where the global fit method extracts a larger oscillation amplitude. From the first Fourier coefficient figure at each energy, the ratio $R_{l,2}^2/R_{l,0}^2$ is systematically further below zero for the global fit method results. This is a systematic difference, independent of centrality and energy, related to the different parameterizations in the two fit methods.

For reasons discussed in Sec. V C, results using the global fit method are not shown for the most central 0-5% data, as well as a few 5-10% cases for 7.7 and 11.5 GeV where the statistics are low. Still, in all cases, the fit projections from the global fit method better match the data, there is better agree-

ment between forward and backward as well as mid-rapidity results and, as discussed in Sec. V C, the errors are not underestimated as they are for the HHLW fit method. Therefore, results using the global fit method are used later when discussing the freeze-out shape.

2. Fourier components

The trends exhibited by the Fourier coefficients are qualitatively similar for all energies. The 0th-order coefficients are consistent with the non-azimuthal results. Like in the non-azimuthal results, the increase of the 0th-order coefficients for more central data is related to the increasing volume of the homogeneity regions in more central events. Since the ratios of 2nd- to 0th-order results are related to the freeze-out shape, the trends are expected to extrapolate toward zero for more central, more round collisions. The right column of the Fourier coefficient figures for each energy demonstrate that this behavior is observed. For each HBT radius, the ratios of 2nd- to 0th-order coefficients follow similar trends for all energies, rapidities, and centralities. This means that the 2nd-order coefficients (half the oscillation amplitudes) have the same sign in all these cases. Therefore, the data requires that all energies, rapidity ranges, and centralities must exhibit oscillations of
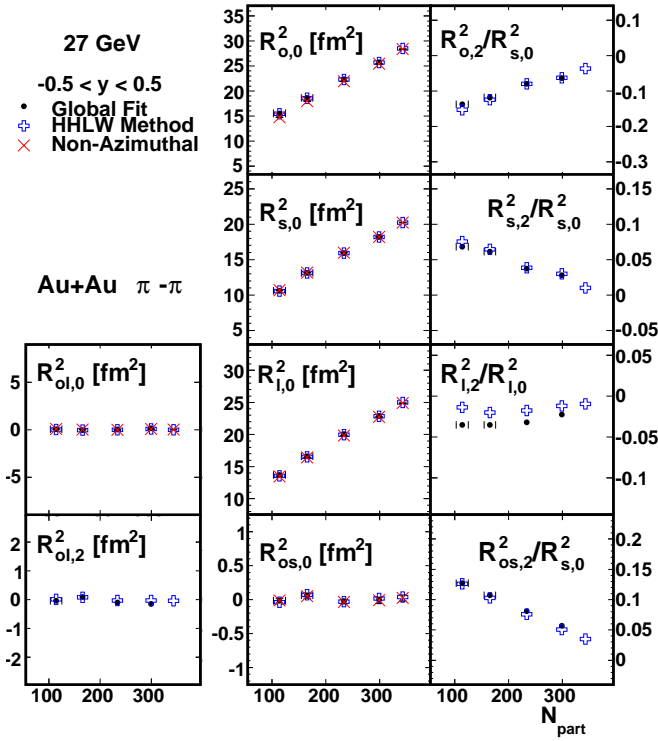
FIG. 18: (Color online) Centrality dependence of the Fourier coefficients that describe azimuthal oscillations of the HBT radii, at mid-rapidity ($-0.5 < y < 0.5$), in 27 GeV collisions with $\langle k_T \rangle \approx 0.31$ GeV/c. The symbols have the same meaning as in Fig. 12. Error bars include only statistical uncertainties. The 0-5% global fit method point is excluded.
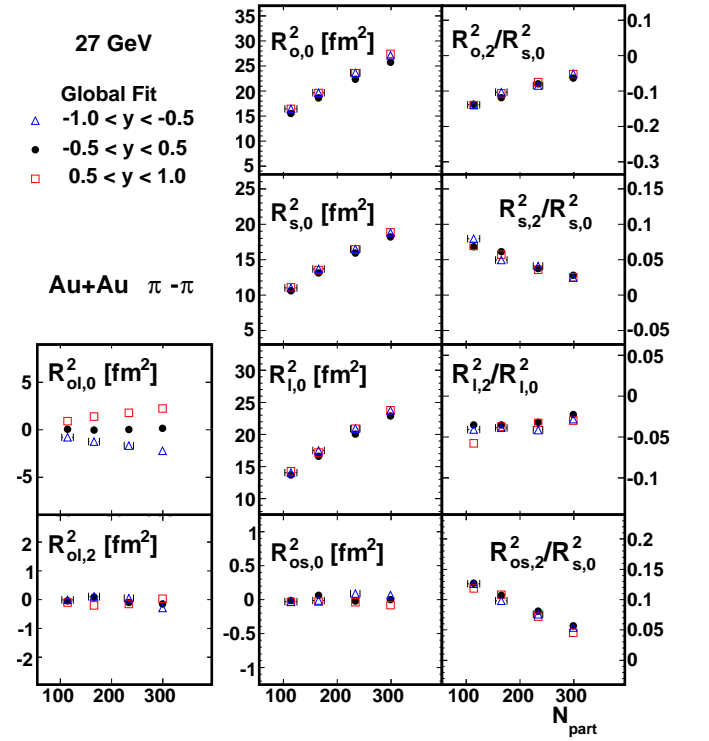
FIG. 19: (Color online) Centrality dependence of the Fourier coefficients that describe azimuthal oscillations of the HBT radii, at backward ($-1 < y < -0.5$), forward ($0.5 < y < 1$) and mid ($-0.5 < y < 0.5$) rapidity, in 27 GeV collisions with $\langle k_T \rangle \approx 0.31$ GeV/c using the global fit method. Error bars include only statistical uncertainties. The 0-5% global fit point is excluded.

the HBT radii that are qualitatively similar to those in Fig. 4. The Fourier coefficients for all three rapidities are similar in most cases, especially in the $R^2_{s,2}/R^2_{s,0}$ values for 10-20% and 20-30% centralities used later in the excitation function for the freeze-out eccentricity.

One interesting feature occurs in the $R^2_{ol,0}$ parameter at forward and backward rapidity. This parameter exhibits both centrality and energy dependence that may be relevant for constraining future model studies. The centrality dependence is shown in the upper panels in the left column of Figs. 13, 15, 17, 19, 21, 23, and 25. As discussed earlier, this term averages to zero for results centered at mid-rapidity, but is otherwise non-zero. At the lowest energy, the $R^2_{ol,0}$ offset is quite large (Fig. 13) and increases in a linear manner with N_{part}. At higher energies, although the linear trend with N_{part} remains, the slope decreases for larger $\sqrt{s_{NN}}$. For the 200 GeV results in Fig. 25, the slope and values are quite small compared to the 7.7 GeV case, for instance. As discussed in Sec. III B, this non-zero cross term corresponds to a tilt in the q_{out}-q_{long} plane. The non-zero value of the cross term means there is a correlation between the relative momentum of particle pairs in the out and long directions.

Two considerations affect how $R^2_{ol,0}$ (or any of the radii) are related to physical parameters of interest. One is the frame in which the correlation function is constructed (fixed center of mass, LCMS, etc.) [52, 74]. The other involves the assumptions that enter a particular analytical model of the source distribution (static, longitudinal flow, transverse flow, boost-invariance, etc.) that is required to relate the extracted fit parameters (radii) to physical quantities such as freeze-out duration or total lifetime [52, 74].

Assume for the moment that radii are measured in the LCMS frame, as in this analysis. In models with longitudinal expansion, breaking of boost-invariance results in non-zero values of the $R^2_{ol,0}$ cross term away from mid-rapidity [52, 74]. The reason is that the LCMS and local rest frame of the source only coincide in the boost-invariant model [74]. This is one example of how changing the model assumptions leads to a different relationship between the radii (including $R^2_{ol,0}$) and physical parameters.

Alternatively, if the same analytical model is assumed but the measurement is performed in different frames, the dependence of the radii on the physical parameters will also change. Ref. [74] demonstrates that, assuming boost invariant longitudinal expansion, measurement in a fixed frame, the LCMS frame, and a generalized Yano-Koonin frame lead to three different relationships between the fit parameters (radii) and physical quantities. In Ref. [52], a similar analytical model leads to a quite complex dependence of $R^2_{ol,0}$ on various physical quantities in the center of mass frame. However, the ex-
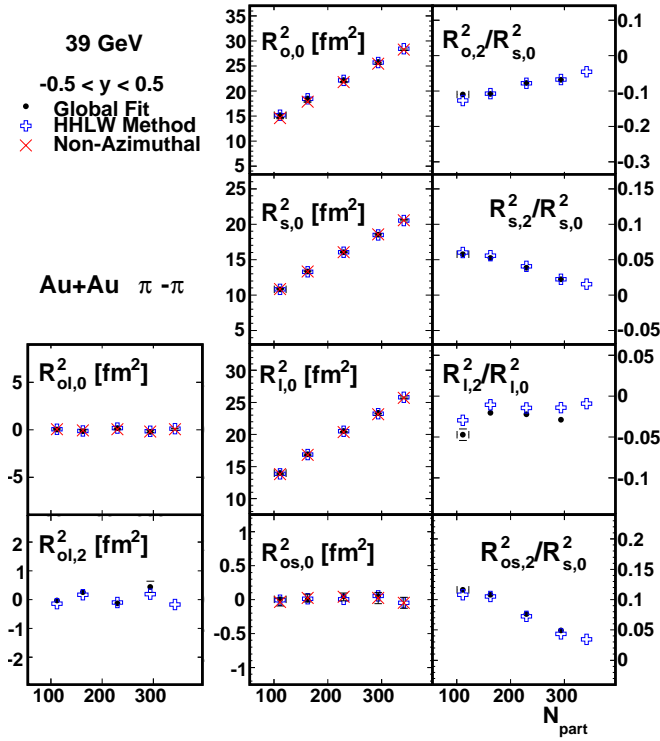
FIG. 20: (Color online) Centrality dependence of the Fourier coefficients that describe azimuthal oscillations of the HBT radii, at mid-rapidity ($-0.5 < y < 0.5$), in 39 GeV collisions with $\langle k_T \rangle \approx 0.31$ GeV/c. The symbols have the same meaning as in Fig. 12. Error bars include only statistical uncertainties. The 0-5% global fit method point is excluded.
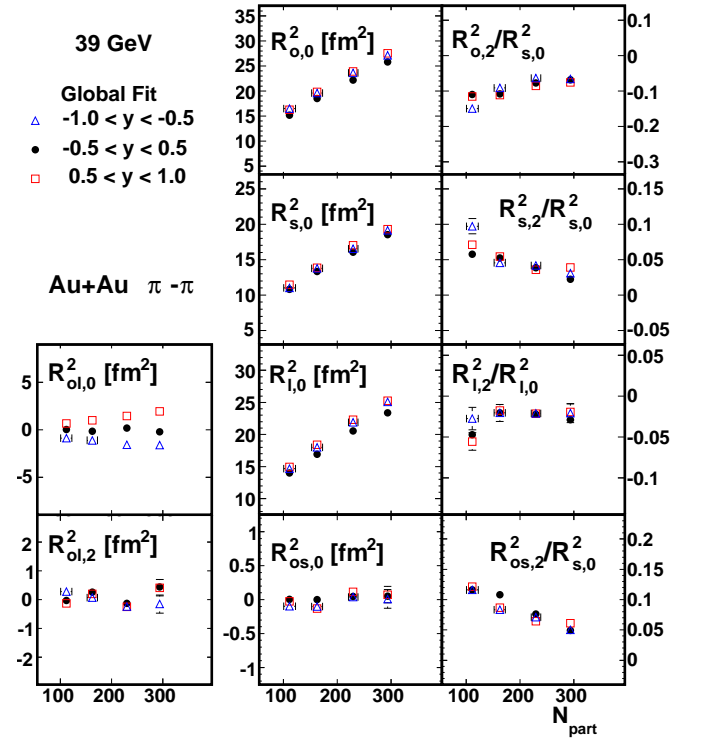
FIG. 21: (Color online) Centrality dependence of the Fourier coefficients that describe azimuthal oscillations of the HBT radii, at backward ($-1 < y < -0.5$), forward ($0.5 < y < 1$) and mid ($-0.5 < y < 0.5$) rapidity, in 39 GeV collisions with $\langle k_T \rangle \approx 0.31$ GeV/c using the global fit method. Error bars include only statistical uncertainties. The 0-5% global fit point is excluded.

pression greatly simplifies in the LCMS frame, leaving $R^2_{ol,0}$ directly proportional to the freeze-out duration and other parameters.

Fig. 26 shows that, for each centrality, $R^2_{ol,0}$ decreases smoothly toward zero at higher collision energy. It has been suggested [52, 74] that the quantity $R^2_{\text{out}} - R^2_{\text{side}}$ is sensitive to the duration of particle emission, $\Delta\tau$, which provided the main motivation for the past studies of $R_{\text{out}}/R_{\text{side}}$, summarized in Fig. 6. The R^2_{ol} offset has also been associated with the duration of freeze-out and other parameters in a mathematically different way [52, 74]. Within the framework of a given model, this new data may allow an estimate of $\Delta\tau$, (and also other parameters described in the references) as a function of beam energy, using a variable that has different dependence on $\Delta\tau$ than does the more commonly studied quantity $R^2_{\text{out}} - R^2_{\text{side}}$.

One other observation can be made because the $R^2_{ol,0}$ values in Fig. 26 are measured in the LCMS frame. As mentioned above, non-zero values of $R^2_{ol,0}$ suggest boost-invariance may be broken. The higher absolute values of $R^2_{ol,0}$ at lower $\sqrt{s_{NN}}$ may thus reflect that the assumption of boost-invariance becomes less valid at lower energies.

3. Kinetic freeze-out eccentricity

Once the Fourier coefficients are extracted the eccentricity, defined as

$$\varepsilon_F = \frac{\sigma'^2_y - \sigma'^2_x}{\sigma'^2_y + \sigma'^2_x} \approx 2\frac{R^2_{s,2}}{R^2_{s,0}} \qquad (20)$$

can be simply computed [23]. The variances σ'_y and σ'_x correspond to the widths of the collision fireball at kinetic freeze-out in the out-of-plane and in-plane directions, respectively. This definition allows negative eccentricities if $\sigma'_y < \sigma'_x$ which would indicate the system expanded enough to become in-plane extended. Whether or not that happens is related to the collision dynamics and equation of state as described in Sec. II. The ratio $R^2_{s,2}/R^2_{s,0}$ is used to estimate ε_F because R_{side} is less affected by flow, and hence it carries primarily geometric information [23].

Figure 27 shows the eccentricities at kinetic freeze-out, ε_F, defined in Eq. 20, for all centralities and energies. They are plotted against the initial eccentricity relative to the participant plane obtained from the Glauber model [49], defined as
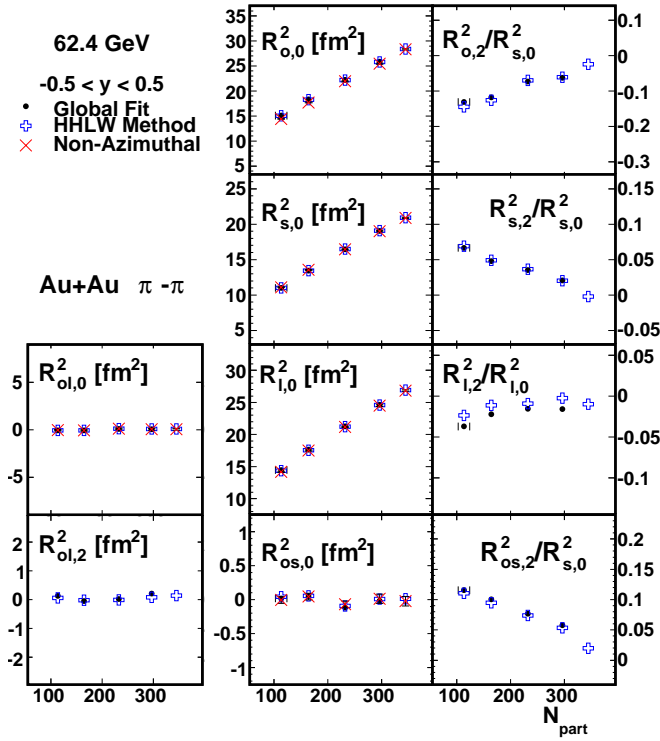
FIG. 22: (Color online) Centrality dependence of the Fourier coefficients that describe azimuthal oscillations of the HBT radii, at mid-rapidity ($-0.5 < y < 0.5$), in 62.4 GeV collisions with $\langle k_T \rangle \approx 0.31$ GeV/c. The symbols have the same meaning as in Fig. 12. Error bars include only statistical uncertainties. The 0-5% global fit method point is excluded.

FIG. 23: (Color online) Centrality dependence of the Fourier coefficients that describe azimuthal oscillations of the HBT radii, at backward ($-1 < y < -0.5$), forward ($0.5 < y < 1$) and mid ($-0.5 < y < 0.5$) rapidity, in 62.4 GeV collisions with $\langle k_T \rangle \approx 0.31$ GeV/c using the global fit method. Error bars include only statistical uncertainties. The 0-5% global fit point is excluded.

$$\varepsilon_{PP} = \frac{\sqrt{(\sigma_y^2 - \sigma_x^2)^2 + 4\sigma_{xy}^2}}{\sigma_x^2 + \sigma_y^2}. \quad (21)$$

The variances $\sigma_x^2 = \{x^2\} - \{x\}^2$ and $\sigma_y^2 = \{y^2\} - \{y\}^2$ gauge the widths of the distributions of participant nucleons in and out of the reaction plane direction, respectively. The symbol $\{\dots\}$ denotes averaging of participant nucleons, with positions x and y, in each event. The covariance $\sigma_{xy} = \{xy\} - \{x\}\{y\}$ accounts for event-by-event fluctuations in the distribution of participant nucleons. The line has a slope of one ($\varepsilon_F = \varepsilon_{PP}$), so points further below the line have evolved more toward a round shape ($\varepsilon_F = 0$). These results demonstrate that, at all energies studied, the freeze-out shape remains an out-of-plane extended ellipse ($\varepsilon_F > 0$). In no case does extended lifetime or stronger flow result in the shape becoming in-plane extended ($\varepsilon_F < 0$). However, there is always some evolution toward a more round shape, as expected, and there tends to be slightly more evolution for the higher energies. The same observations apply at forward and backward rapidity because of the similar trends observed for the ratio $R_{s,2}^2/R_{s,0}^2$ ($= \varepsilon_F/2$).

The excitation function for the freeze-out shape is presented in Fig. 28. The new STAR results for three rapidities are compared to earlier measurements from other experiments and to several models. The results use the global fit method and
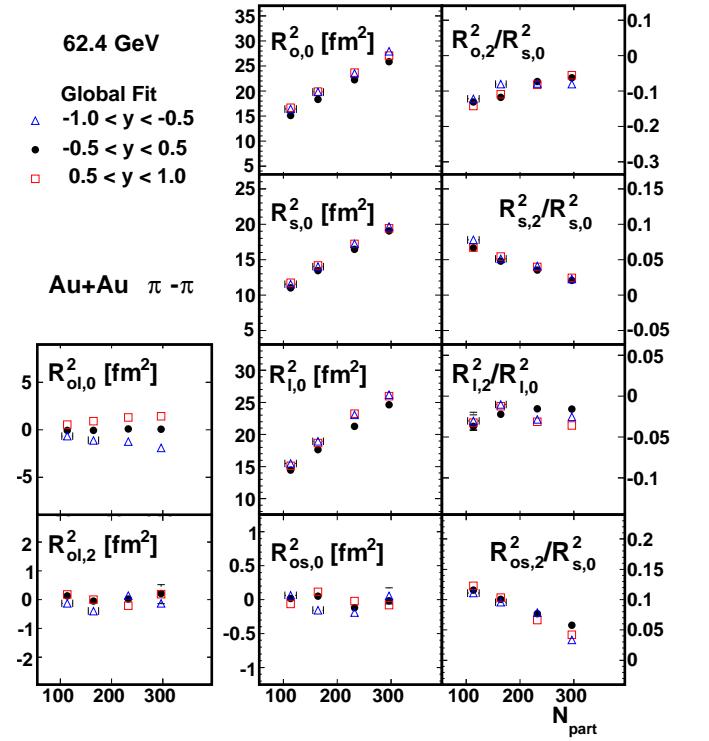
are for mid-peripheral (10-30%) collisions where the initial anisotropic shape is large but there is still significant overlap of the nuclei. The larger differences between in-plane and out-of-plane pressure gradients in these collisions and larger initial spatial anisotropy could admit more varied results in the change in shape, if that where to happen at different energies. The new STAR results exhibit a monotonic decrease in the freeze-out eccentricity with increasing beam energy for all three rapidity regions.

The freeze-out eccentricity values from CERES and STAR at similar energy and centrality are not consistent. There are some differences in analyses from these different experiments such as correction for event plane resolution, fitting in one k_T bin versus averaging several smaller k_T bins, and centrality ranges. These could potentially be important and were studied. The CERES point at 17.3 GeV suggested a possible minimum in the historical data. The new STAR results at 11.5 and 19.6 GeV at mid-rapidity were significantly higher suggesting a monotonic decrease in the freeze-out shape. To check that the difference was not due to the different rapidity windows the STAR analysis was extended to include the same rapidity region as CERES, $0.5 < |y| < 1$. The forward and backward rapidity results remained consistent with the mid-rapidity measurement. The CERES point for 10-25% centrality is consistent with the (smaller) eccentricities for the 0-5%
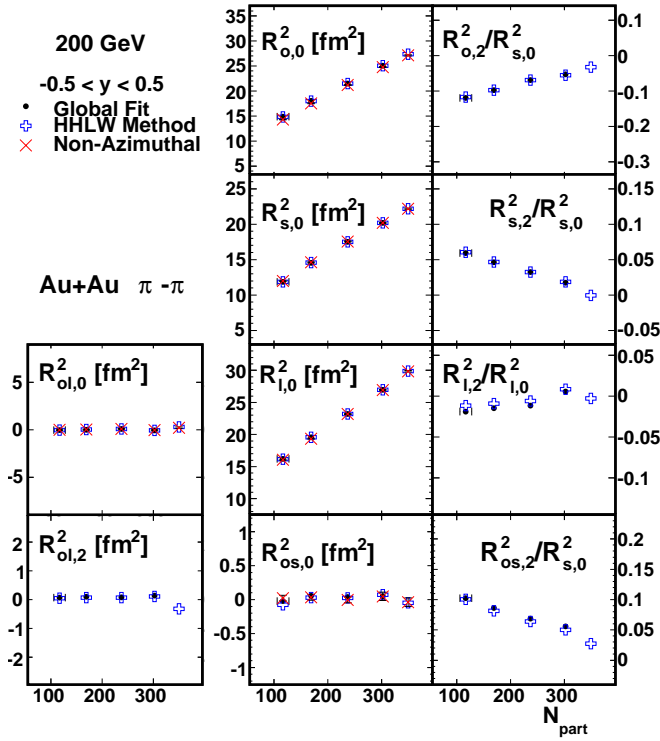
FIG. 24: (Color online) Centrality dependence of the Fourier co-efficients that describe azimuthal oscillations of the HBT radii, at mid-rapidity ($-0.5 < y < 0.5$), in 200 GeV collisions with $\langle k_T \rangle \approx 0.31$ GeV/c. The symbols have the same meaning as in Fig. 12. Error bars include only statistical uncertainties. The 0-5% global fit method point is excluded.

FIG. 25: (Color online) Centrality dependence of the Fourier coeffi-cients that describe azimuthal oscillations of the HBT radii, at back-ward ($-1 < y < -0.5$), forward ($0.5 < y < 1$) and mid ($-0.5 < y < 0.5$) rapidity, in 200 GeV collisions with $\langle k_T \rangle \approx 0.31$ GeV/c using the global fit method. Error bars include only statistical uncertain-ties. The 0-5% global fit point is excluded.

and 5-10% centrality ranges in STAR results at 19.6 GeV, so it seems rather unlikely that large enough differences in cen-trality definitions could occur to cause such a large difference in the eccentricities for STAR and CERES. Event, track, and pair selection quantities have rather little effect on the results. Another difference is the range of k_T values included in the fits. In the CERES and earlier STAR result [40], the azimuthal analysis was done in narrow k_T bins and the ε_F values aver-aged. This was problematic at the lowest energies due to lower statistics when the analysis was additionally differential in k_T. Using a single, wide k_T bin biases the results slightly toward smaller ε_F values, as discussed in Sec. III D. Therefore, to be consistent, the same (wide k_T bin) method is used for all the STAR points. The CERES results used a weighted average of results in narrow k_T bins which should be equivalent to using a single, wide k_T bin. It seems unlikely that this is the cause of the discrepency. The E895 correction algorithm was used in the CERES and E895 cases to correct for the event plane res-olution while in the STAR case the histograms were corrected or the fit function smeared in the global fit case. The differ-ence in the results is rather tiny for these different methods and also cannot explain the difference.

As discussed in Sec. II, non-monotonic behavior in the ex-citation function would have strongly suggested interesting changes in the equation of state. The observed monotonic de-
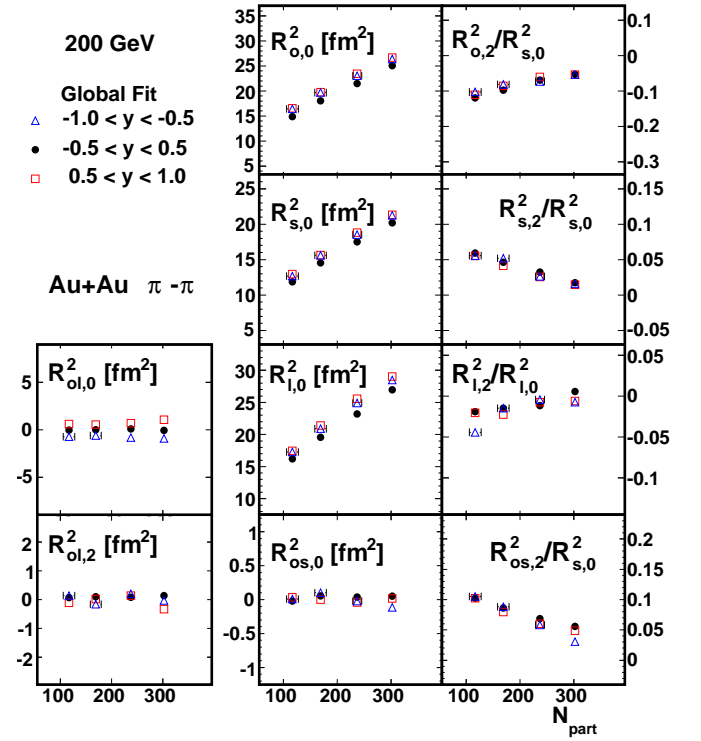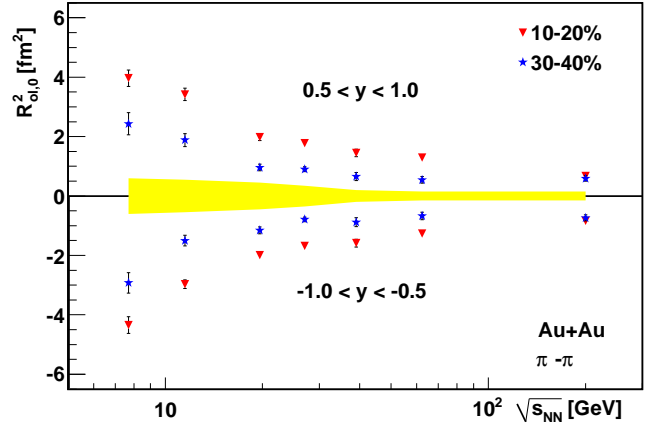

FIG. 26: (Color online) Beam energy dependence of the $R_{ol,0}^2$ cross term for forward and backward rapidity with $\langle k_T \rangle \approx 0.31$ GeV/c. The yellow band shows estimated systematic uncertainty.

crease excludes the scenario described in reference [19] and is consistent with increased lifetime and/or pressure gradients at higher energy. The energy dependence of R_{long} from the non-azimuthal analysis, and the lifetimes shown in Fig. 11, suggest also that the system is longer-lived at higher energy. Still, these results will allow to probe equation of state effects
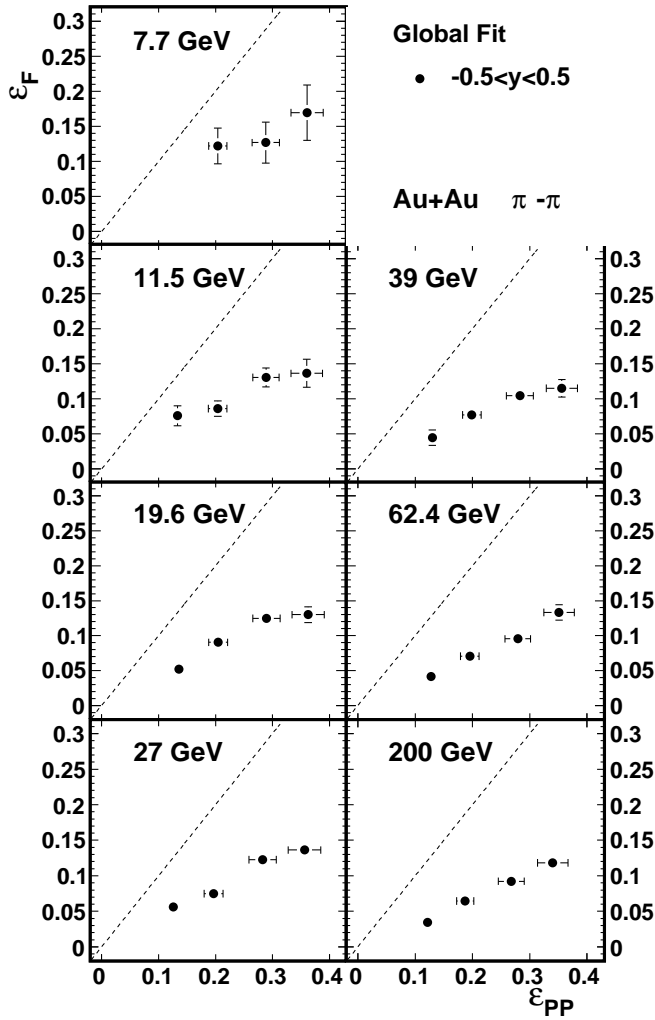
FIG. 27: The eccentricity of the collisions at kinetic freez-out, ε_F, as a function of initial eccentricity relative to the participant plane, ε_{PP}, at mid-rapidity. All results are for $\langle k_T \rangle \approx 0.31$ GeV/c. Error bars include only statistical uncertainties. The line has a slope of one indicating no change in shape. Points further below the line evolve more to a round shape.

by comparing to various models.

The currently available model predictions [19, 45, 75] for the energy dependence of the freeze-out eccentricity are also shown in Fig. 28. All models predict a monotonic decrease in the freeze-out shape at higher energies similar to the data. The older (2+1)D, ideal hydrodynamical models [45], labeled EOS-H, EOS-I, and EOS-Q, all overpredict the data. As was noted in [75], in comparison to the historical data, the model with a first order phase transition, EOS-Q, gets close to the 200 GeV point. The predictions of the freeze-out shape are sensitive to the equation of state used in the hydrodynamic models. This is clear by comparing the curves for EOS-I (ideal, massless quark gluon gas) and EOS-H (hadronic gas). For EOS-Q, the slope changes, following EOS-H at low energies, but dropping more rapidly at higher energies. This is attributed to passage through a mixed-phase regime which

extends the lifetime allowing the system to evolve to a more round state at higher energies [19].

The two more recent (2+1)D predictions, from the VISH2+1 model, get closer to the data. MC-KLN and MC-GLB correspond to different initial conditions and are more realistic than the earlier results as they allow to incorporate viscous effects [75]. MC-GLB uses a specific shear viscosity of $\eta/s = 0.08$ with Glauber initial conditions. The MC-KLN model has a much larger specific shear viscosity, $\eta/s = 0.2$, and the initial shape is derived from the initial gluon density distribution in the transverse plane (which is converted to an entropy and finally energy density profile). Both models incorporate an equation of state based on lattice QCD, named s95p-PCE [76, 77]. Initial parameters in the models were calibrated using measured multiplicity distributions (and extrapolations to lower energies) and to describe p_T-spectra and v_2 measurements for 200 GeV Au+Au collisions at RHIC. The two cases were found to yield similar lifetimes, but in the MC-KLN case the initial eccentricities are larger (more out-of-plane extended). The MC-KLN model achieves a less round shape simply because it starts with larger initial eccentricity [75]. The excitation function for freeze-out eccentricities has the potential to resolve ambiguities between models with different initial conditions and values of η/s. In particular, the two sets of initial conditions and η/s used here yield identical v_2, but very different ε_F. So the results in Fig. 28 provide tighter constraints on these models.

The goal of [75] was to map systematic trends in observables with the two models, not to explain the data precisely. In fact, the applicability of these models is known to be problematic at lower energies both because they assume boost-invariance, which is broken at lower energy, and because the hadronic phase is expected to become more important at lower collision energy. A more realistic calculation requires (3+1)D viscous hydrodynamics. Nevertheless, the new calculations are able to match more closely the experimental results. Of the hydrodynamical models, MC-GLB is closest to the data although it still overpredicts the freeze-out eccentricity and the slope appears too steep. One relevant observation from [75] is that in these models the decrease in the eccentricity with energy appears to be due mainly to an extended lifetime rather than larger anisotropy of pressure gradients. As discussed at the end of Sec. VI A, the lifetime extracted from R_{long} values also suggest an increase in the total lifetime. However, the data cannot allow one to determine whether the decrease in eccentricity is due solely to increased lifetime or whether the pressure gradients may also play a significant role.

The prediction of the Boltzmann transport model, UrQMD (v2.3) [78], matches most closely the freeze-out shape at all energies [19]. UrQMD follows the trajectories and interactions of all hadronic particles throughout the collision, so it does not require assumptions about how freeze-out occurs. The model is 3D and does not require boost-invariance, therefore it is equally applicable at all the studied energies. This may be, at least partially, why the predictions from UrQMD more closely match the energy dependence of the data compared to the hydrodynamic predictions. While it does not explicitly contain a deconfined state, it does incorporate color
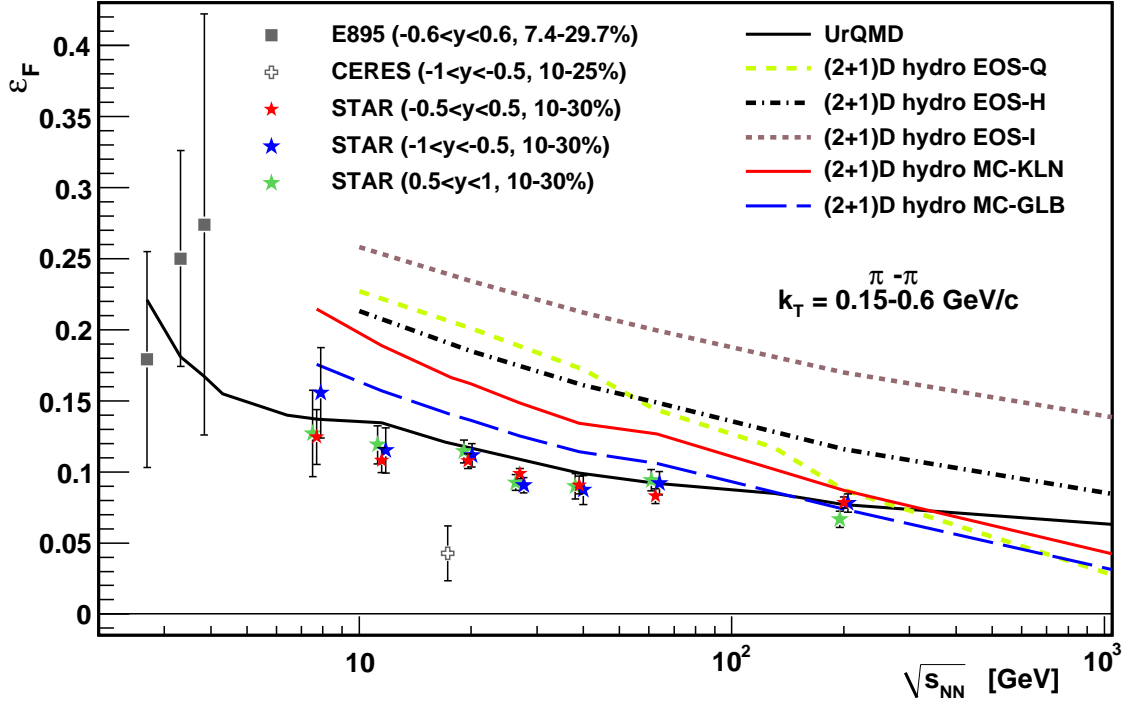
FIG. 28: (Color online) The dependence of the kinetic freeze-out eccentricity of pions on collision energy in mid-central Au+Au collisions (E895, STAR) and Pb+Au collisions (CERES) for three rapidity regions and with $\langle k_T \rangle \approx 0.31$ GeV/c. For clarity, the points for forward and backward rapidity from STAR are offset slightly. Error bars include only statistical uncertainties. Several (2+1)D hydrodynamical models and UrQMD calculations are shown. Model centralities correspond to the data. The trend is consistent with a monotonic decrease in eccentricity with beam energy. Systematic measurement uncertainty on ε is about the size of the datapoints (0.005) and independent of $\sqrt{s_{NN}}$. This systematic uncertainty is significantly smaller than statistical uncertainties and so is not drawn, to reduce clutter.

degrees of freedom through inclusion of the creation of color strings and their subsequent decay back into hadrons.

For the azimuthally integrated results, UrQMD does rather well at predicting the observed dependence of HBT radii on $\langle k_T \rangle$ and centrality [79, 80]. As discussed earlier, inclusion of a mean field acting between pre-formed hadrons (color string fragments) predicts R_{out}/R_{side} ratios similar to the observed values and leads naturally to a minimum in the volume similar to that which is observed experimentally [72, 73]. Such a repulsive potential between the string fragments would mimic somewhat an increase in pressure gradients at early stages [73] similar to the hydrodynamics cases with an equation of state that includes a phase transition. The UrQMD predictions for the eccentricities at kinetic freeze-out in Fig. 28 were made with UrQMD in cascade mode and so do not incorporate this potential between string fragments.

It should be noted that none of the models predict all observables simultaneously. The UrQMD model, while it matches the freeze-out shapes well, matches the momentum space observables less well [82, 83]. And the hydrodynamic models, while they are able to describe the momentum space p_T spectra and v_2 results, do less well at predicting the eccentricity and trends observed in HBT analyses [22, 75]. The availability of these new experimental results provide an important opportunity to further constrain models.

VII. CONCLUSIONS

The two-pion HBT analyses that have been presented provide key measurements in the search for the onset of a first-order phase transition in Au+Au collisions as the collision energy is lowered. The Beam Energy Scan program has allowed HBT measurements to be carried out across a wide range of energies with a single detector and identical analysis techniques. In addition to standard azimuthally integrated measurements, we have performed comprehensive, high precision, azimuthally sensitive femtoscopic measurements of like-sign pions. In order to obtain the most reliable estimates of the eccentricity of the collisions at kinetic freeze-out, a new global fit method has been developed.

A wide variety of HBT measurements have been performed and the comparison of results at different energies is greatly improved. In the azimuthally integrated case, the beam energy dependence of the radii generally agree with results from other experiments, but show a much smoother trend than the earlier data which were extracted from a variety of experiments with variations in analysis techniques. The current analyses additionally contribute data in previously unexplored regions of collision energy. The transverse mass dependence is also consistent with earlier observations and allows one to conclude that all k_T and centrality bins exhibit similar trends as a function of collision energy.

The energy dependence of the volume of the homogeneity regions is consistent with a constant mean free path at freeze-out, as is the very flat energy dependence of R_{out}. This scenario also explains the common dependence of R_{side} and R_{long} on the cube root of the multiplicity that is observed at higher energy. For 7.7 and 11.5 GeV, R_{side} appears to deviate slightly from the trend at the higher energies. Two physical changes that may potentially be related to this are the effects of strangeness enhancement (not included in the argument for a constant mean free path at freeze-out) and the rapid increase in the strength of v_2 that levels off around 7.7 to 11.5 GeV. Both of these physical changes occur in the vicinity of the minimum. A systematic study with a single detector at slightly lower energies would be needed to help disentangle the different effects.

The UrQMD model provides an alternative explanation for the minimum in the volume measurement in terms of a change from a hadronic to a partonic state. Including interactions between color string fragments early in the collision, it not only can explain the minimum in the volume, but is also able to find $R_{\text{out}}/R_{\text{side}}$ values close to unity as observed from AGS through RHIC energies and improves the agreement between UrQMD and other observables at the same time. It is interesting that such an interaction potential may somewhat mimic an increase in the pressure gradients, which may correlate with the observation that v_2 increases rapidly with $\sqrt{s_{NN}}$ in this region also.

The lifetime of the collision evolution was extracted using the $\langle m_T \rangle$ dependence of R_{long}. Subject to certain assumptions, the lifetime increases by a factor 1.7 from AGS to 200 GeV collisions measured at STAR. The lifetime increases by about 1.4 times more between RHIC and the LHC. The magnitude of the increased lifetime effect is well beyond systematic measurement uncertainties.

A new global fit method was developed and studied in relation to the HHLW fit method. For most centralities, this method is found to yield more reliable results in cases of low statistics and poor event plane resolution, although it has problems in the most central bin related to different parameterizations. As discussed in section V C, the global fit has the additional benefit that each q-bin for all correlation functions is used precisely once in the fit to extract the parameters $R^2_{\mu,n}$. This eliminates issues with correlated errors that arise when q-bins from correlation functions at all Φ values are used to correct for reaction plane resolution in the HHLW approach. This global fit method has allowed the extraction of the most reliable results at the lowest energies studied.

The Fourier coefficients measured away from mid-rapidity allow one to extract the energy dependence of the $R^2_{ol,0}$ cross term. This previously unavailable observable exhibits a monotonic decrease as a function of beam energy. This observable has been connected to the duration of particle emission in a way that is different than the more commonly studied quantities $R^2_{\text{out}} - R^2_{\text{side}}$ or $R_{\text{out}}/R_{\text{side}}$. This measurement may provide constraints for models that relate the radii and physical quantities with different sets of assumptions.

The azimuthally differential results show that, for all energies, the system remains out of plane extended at freeze-out, despite the evolution of the collision eccentricity." In mid-central (10-30%) collisions, the freeze-out eccentricity shows a monotonic decrease with beam energy consistent with expectations of increased flow and/or increased lifetime at higher energies. This is supported by the azimuthally integrated results which suggest longer lifetimes at higher energies. The results are consistent qualitatively with the monotonic decrease suggested by all model predictions, but is most consistent quantitatively with UrQMD. While the hydrodynamic models can match momentum space observables (p_T spectra, v_2) well, they do less well at predicting the HBT results. At the same time, while the UrQMD model does better at predicting the HBT results, like the freeze-out shape, it does less well at predicting the momentum space observables. The freeze-out eccentricity excitation function provides new, additional information that will help to constrain future model investigations.

Appendix: Non-Gaussian effects on azimuthal HBT analyses

In azimuthally integrated HBT analyses, the cross terms (R_{os}, R_{ol}, R_{sl}) vanish at mid-rapidity. In this case, the sign of the components of the relative momentum vector, $\vec{q}$, are arbitrary. The three dimensional $\vec{q}$-space distributions (numerator, denominator, and Coulomb weighted distributions) may be folded, so that q_{long} and q_{side} are always positive, for instance, to increase statistics in each (q_{out},q_{side},q_{long}) bin. In azimuthally differential analyses, however, the relative signs of components are important in order to extract non-zero cross terms [33, 81]. At mid-rapidity, the relative sign of q_{out} and q_{side} must thus be maintained to extract values of R^2_{os}. Away from mid-rapidity, the R^2_{ol} cross term is also non-zero and q_{long} must be allowed to have both positive or negative values. This way the relative sign of q_{out} and q_{long} is maintained and the corresponding cross term can be extracted.

If the "q-folding" procedure is performed and the cross terms are included as fit parameters, the fit parameters become strongly correlated and the values of the extracted radii change. The size of this effect varies randomly from one azimuthal bin to the next, causing large variations in the extracted oscillations of the radii. This behavior is related to the non-Gaussianess of the correlation function. Due to the necessity of using finite bins in k_T and centrality, which are described by a range of radii, the radii extracted from these correlation functions are some average value. If too much q-folding is performed the signs of the relative momentum components are lost. In cases where the cross terms associated with these relative momentum components are non-zero, the covariance of fit parameters that appears allows deviations from the average values and the results become unreliable.

This is an important consideration for any HBT analysis performed away from mid-rapidity, or relative to the first order reaction plane, where measurement of cross terms is important. In this analysis, no folding of $\vec{q}$-space is performed and so any possible effects of this phenomena are eliminated.

[1] M. M. Aggarwal et al. (STAR Collaboration) (2010), arXiv:1007.2613.

[2] J. Adams et al. (STAR Collaboration), Nucl. Phys. A **757**, 102 (2005).

[3] K. Adcox et al. (PHENIX Collaboration), Nucl. Phys. A **757**, 184 (2005).

[4] B. B. Back et al. (PHOBOS Collaboration), Nucl. Phys. A **757**, 28 (2005).

[5] I. Arsene et al. (BRAHMS Collaboration), Nucl. Phys. A **757**, 1 (2005).

[6] F. R. Brown, F. P. Butler, H. Chen, N. H. Christ, Z. Dong, W. Schaffer, L. I. Unger, and A. Vaccarino, Phys. Rev. Lett. **65**, 2491 (1990).

[7] Y. Aoki, G. Endrodi, Z. Fodor, S. Katz, and K. Szabo, Nature **443**, 675 (2006).

[8] S. Borsanyi et al. (Wuppertal-Budapest Collaboration), JHEP **09**, 073 (2010).

[9] M. Cheng (HotQCD Collaboration), PoS **LAT2009**, 175 (2009).

[10] A. Masayuki and Y. Koichi, Nucl. Phys. A **504**, 668 (1989).

[11] A. Barducci, R. Casalbuoni, G. Pettini, and R. Gatto, Phys. Rev. D **49**, 426 (1994).

[12] J. Berges and K. Rajagopal, Nucl. Phys. B **538**, 215 (1999).

[13] M. A. Halasz, A. D. Jackson, R. E. Shrock, M. A. Stephanov, and J. J. M. Verbaarschot, Phys. Rev. D **58**, 096007 (1998).

[14] O. Scavenius, A. Mócsy, I. N. Mishustin, and D. H. Rischke, Phys. Rev. C **64**, 045202 (2001).

[15] N. G. Antoniou and A. S. Kapoyannis, Phys. Lett. B **563**, 165 (2003).

[16] Y. Hatta and T. Ikeda, Phys. Rev. D **67**, 014028 (2003).

[17] M. Stephanov, Prog. Theor. Phys. Supplement **153**, 139 (2004).

[18] J. Randrup, Phys. Rev. C **82**, 034902 (2010).

[19] M. A. Lisa, E. Frodermann, G. Graef, M. Mitrovski, E. Mount, H. Petersen, and M. Bleicher, New J. Phys. **13**, 065006 (2011).

[20] R. H. Brown and R. Q. Twiss, Nature **178**, 1046 (1956).

[21] G. Goldhaber, S. Goldhaber, W. Lee, and A. Pais, Phys. Rev. **120**, 300 (1960).

[22] M. A. Lisa, S. Pratt, R. Soltz, and U. Wiedemann, Ann. Rev. Nucl. Part. Sci. **55**, 357 (2005).

[23] F. Retière and M. A. Lisa, Phys. Rev. C **70**, 044907 (2004).

[24] E. Mount, G. Graef, M. Mitrovski, M. Bleicher, and M. A. Lisa, Phys. Rev. C **84**, 014908 (2011).

[25] L. Ahle et al. (E-802 Collaboration), Phys. Rev. C **66**, 054906 (2002).

[26] M. A. Lisa et al. (E895 Collaboration), Phys. Rev. Lett. **84**, 2798 (2000).

[27] R. A. Soltz, M. Baker, and J. H. Lee (E866 Collaboration), Nucl. Phys. A **661**, 439 (1999).

[28] D. Adamová et al. (CERES Collaboration), Nucl. Phys. A **714**, 124 (2003).

[29] I. G. Bearden et al. (NA44 Collaboration), Phys. Rev. C **58**, 1656 (1998).

[30] C. Alt et al. (NA49 Collaboration), Phys. Rev. C **77**, 064908 (2008).

[31] M. M. Aggarwal et al. (WA98 Collaboration), Phys. Rev. C **67**, 014906 (2003).

[32] B. B. Back et al. (PHOBOS Collaboration), Phys. Rev. C **73**, 031901 (2006).

[33] J. Adams et al. (STAR Collaboration), Phys. Rev. C **71**, 044906 (2005).

[34] B. I. Abelev et al. (STAR Collaboration), Phys. Rev. C **80**, 024905 (2009).

[35] M. M. Aggarwal et al. (STAR Collaboration), Phys. Rev. C **83**, 064905 (2011).

[36] K. Aamodt et al. (ALICE Collaboration), Phys. Lett. B **696**, 328 (2011).

[37] A. Kisiel (ALICE Collaboration), J. Phys. G **38**, 124008 (2011).

[38] J. L. Gramling (ALICE Collaboration), AIP Conf. Proc. **1422**, 68 (2012).

[39] M. A. Lisa et al. (E895 Collaboration), Phys. Lett. B **496**, 1 (2000).

[40] J. Adams et al. (STAR Collaboration), Phys. Rev. Lett. **93**, 012301 (2004).

[41] A. Adare et al. (PHENIX Collaboration), Phys. Rev. Lett. **112**, 222301 (2014).

[42] D. Adamová et al. (CERES Collaboration), Phys. Rev. C **78**, 064901 (2008).

[43] B. Alver and G. Roland, Phys. Rev. C **81**, 054905 (2010).

[44] C. Hung and E. V. Shuryak, Phys. Rev. Lett. **75**, 4003 (1995).

[45] P. F. Kolb and U. W. Heinz (2003), arXiv:nucl-th/0305084.

[46] K. H. Ackermann et al. (STAR Collaboration), Nucl. Instrum. Methods A **499**, 624 (2003).

[47] M. Anderson et al. (STAR collaboration), Nucl. Instrum. Methods A **499**, 659 (2003).

[48] K. H. Ackermann et al., Nucl. Phys. A **661**, 681 (1999).

[49] L. Adamczyk et al. (STAR collaboration), Phys. Rev. C **86**, 054908 (2012).

[50] S. Pratt, Phys. Rev. D **33**, 1314 (1986).

[51] G. Bertsch, M. Gong, and M. Tohyama, Phys. Rev. C **37**, 1896 (1988).

[52] S. Chapman, P. Scotto, and U. Heinz, Phys. Rev. Lett. **74**, 4400 (1995).

[53] U. Heinz, A. Hummel, M. A. Lisa, and U. A. Wiedemann, Phys. Rev. C **66**, 044903 (2002).

[54] M. G. Bowler, Phys. Lett. B **270**, 69 (1991).

[55] Y. M. Sinyukov, R. Lednicky, S. Akkelin, J. Pluta, and B. Erazmus, Phys. Lett. B **432**, 248 (1998).

[56] W. A. Zajc et al., Phys. Rev. C **29**, 2173 (1984).

[57] H. W. Barz, Phys. Rev. C **59**, 2214 (1999).

[58] A. M. Poskanzer and S. A. Voloshin, Phys. Rev. C **58**, 1671 (1998).

[59] J. Barrette et al. (E877 Collaboration), Phys. Rev. C **55**, 1420 (1997).

[60] H. Appelshäuser et al. (NA49 Collaboration), Phys. Rev. Lett. **80**, 4136 (1998).

[61] P. Danielewicz et al., Phys. Rev. C **38**, 120 (1988).

[62] J. Barrette et al., Phys. Rev. C **56**, 3254 (1997).

[63] D. H. Rischke and M. Gyulassy, Nucl. Phys. A **608**, 479 (1996).

[64] U. W. Heinz and P. F. Kolb (2002), arXiv:hep-ph/0204061.

[65] M. Herrmann and G. Bertsch, Phys. Rev. C **51**, 328 (1995).

[66] U. A. Wiedemann, P. Scotto, and U. Heinz, Phys. Rev. C **53**, 918 (1996).

[67] A. N. Makhlin and Y. M. Sinyukov, Z. Phys. C **39**, 69 (1988).

[68] D. Adamová et al. (CERES Collaboration), Phys. Rev. Lett. **90**, 022301 (2003).

[69] C. Alt et al. (NA49 Collaboration), Phys. Rev. C **77**, 024903 (2008).

[70] K. Aamodt et al. (ALICE Collaboration), Phys. Rev. Lett. **105**, 252302 (2010).

[71] L. Adamczyk et al. (STAR collaboration), Phys. Rev. C **86**, 054908 (2012).

[72] Q. Li, C. Shen, and M. Bleicher (2010), arXiv:1009.3334.

[73] Q. Li, M. Bleicher, and H. Stocker, Phys. Lett. B **659**, 525 (2008).

[74] S. Chapman, J. R. Nix, and U. Heinz, Phys. Rev. C **52**, 2694 (1995).

[75] C. Shen and U. Heinz, Phys. Rev. C **85**, 054902 (2012).

[76] C. Shen, U. Heinz, P. Huovinen, and H. Song, Phys. Rev. C **82**, 054904 (2010).

[77] P. Huovinen and P. Petreczky, Nucl. Phys. A **837**, 26 (2010).

[78] H. Petersen, M. Bleicher, S. A. Bass, and H. Stocker (2008), arXiv:0805.0567.

[79] Q. Li, M. Bleicher, and H. Stoecker, Phys. Rev. C **73**, 064908 (2006).

[80] Q. Li, M. Bleicher, X. Zhu, and H. Stocker, J. Phys. G **34**, 537 (2007).

[81] R. Wells, Ph.D. thesis, The Ohio State University (2002).

[82] L. Adamczyk et al. (STAR collaboration), Phys. Rev. Lett. **112**, 162301 (2014).

[83] L. Adamczyk et al. (STAR collaboration), Phys. Rev. C **88**, 14902 (2013).

[84] U. W. Heinz, B. Tomasik, U. A. Wiedemann and Y. F. Wu, Phys. Lett. B **382**, 181 (1996) [nucl-th/9603011].

[85] S. Soff, S. A. Bass and A. Dumitru, Phys. Rev. Lett. **86**, 3981 (2001) [nucl-th/0012085].

[86] We thank Roy Lacey for prompting us to re-examine the transverse radii measured at RHIC and LHC, separate from older data.

[87] L. Adamczyk *et al.* [STAR Collaboration], Phys. Rev. Lett. **113**, 052302 (2014) [arXiv:1404.1433 [nucl-ex]].

[88] L. Adamczyk *et al.* [STAR Collaboration], Phys. Rev. Lett. **112**, 162301 (2014) [arXiv:1401.3043 [nucl-ex]].

[89] L. Adamczyk *et al.* [STAR Collaboration], Phys. Rev. Lett. **112**, no. 3, 032302 (2014) [arXiv:1309.5681 [nucl-ex]].

[90] L. Adamczyk *et al.* [STAR Collaboration], Phys. Rev. Lett. **110**, 142301 (2013) [arXiv:1301.2347 [nucl-ex]].